Turbulence in Superfluid ^{4}He Films around Substrate Defects

by

Joseph Natter
Class of 2017

A thesis (or essay) submitted to the
faculty of Wesleyan University
in partial fulfillment of the requirements for the
Degree of Bachelor of Arts
with Departmental Honors in Physics

Abstract:

This thesis seeks to help explain dissipation observed in third sound Superfluid ^{4}He by the Quantum Fluids Group at Wesleyan. Turbulence is a common hypothesis for these types of dissipation; however, it is not well understood how vortices form and nucleate in Superfluid. This project examines possible vortex formation conditions around surface defects: obstructions and bumps. We have solved for the flow fields of vortex pairs around defects, found the energy costs to vortex pair nucleation around these defects, and shown that energy cost for pair nucleation is lower for larger defects in higher velocities. Along with microscopic measurements of superfluid resonator surface defects, this model should be able to confirm whether or not observed dissipation is resulting from vortex pair formation around surface defects.

Acknowledgements

Table of Contents

Chapter 1: Background

This chapter describes superfluid structure, quantum vortices, and image solutions to Laplace's equation.

Chapter 2: Obstruction to flow

This chapter investigates vortex pair behavior around a complete obstruction to flow. Energy of a vortex pair is calculated, and the energy barrier to nucleation is analyzed in terms of the size of the obstruction and strength of background flow.

Chapter 3: Spherical bump

This chapter investigates vortex pair behavior around a spherical bump that permits flow over its surface. A series of vortex images is constructed to solve Laplace's equation, energy of a pair is calculated, and the energy barrier to nucleation is analyzed.

Chapter 4: Conclusion

This chapter attempts to draw conclusions from our investigations, and lays out potential next steps.

Chapter 1: Background

Superfluid Structure

When ^{4}He is cooled beneath the λ point of 2.17 K, it enters into the Helium II superfluid state. In this superfluid state, all of the Helium atoms, which are bosons, enter into an identical quantum ground state, or thermodynamic quasi-ground state. Above absolute zero, however, there will be thermal fluctuations superimposed on this ground state behavior. The total superfluid wavefunction can be separated into the superfluid quasi-ground state and a thermal excitation component:

$$\Psi = \Psi_0 + \sum_n \phi_n \tag{1}$$

Where Ψ_0 is the quasi-ground state, and each ϕ_n is a thermal excitation. The quasi-ground state need not actually be the single lowest energy state possible for the system; it just refers to a single Hamiltonian eigenstate that will not change from thermal fluctuations on a relevant time scale.

Landau modeled this as a two fluid system - a system consisting of the quantum superfluid component as well as a normal fluid composed of thermal excitations. [A.]
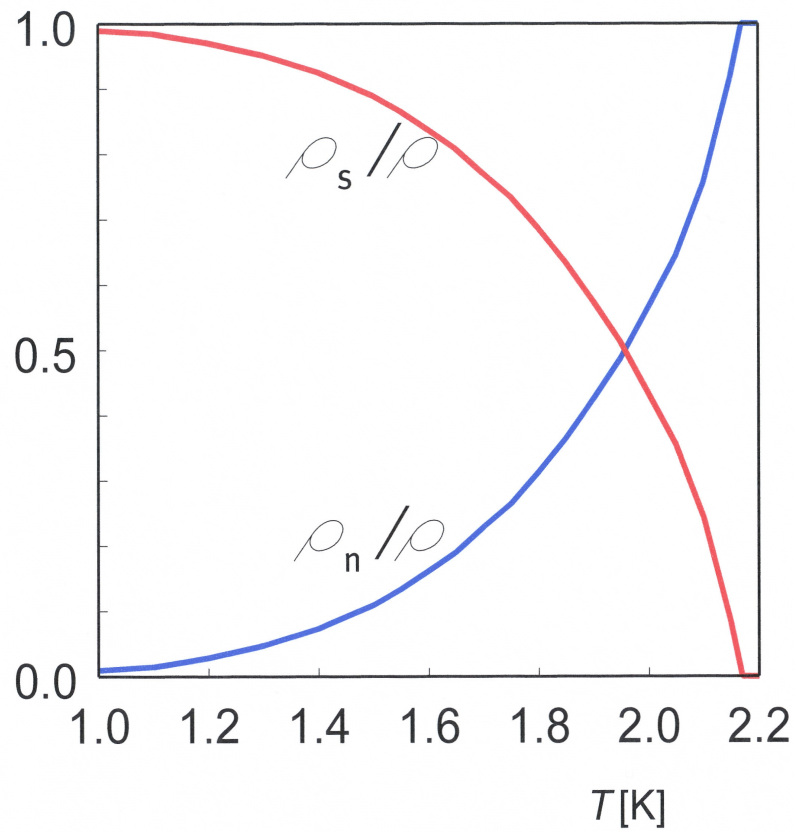
Figure 1.1: Temperature dependence of the superfluid and normal components of Helium II. ρ_s is the density of the superfluid component, ρ_n is the density of the normal fluid component [A.]

For this project, we are interested in examining the behavior of Helium II in the low temperature limit; that is to say, $\frac{\rho_s}{\rho} \simeq 1$. Under such conditions, T $\simeq 0$ K. This corresponds to a temperature region past the far left side of Figure 1.1. We will not be investigating thermal excitations, only quantum mechanical structures that appear in the wavefunctions of all particles in the superfluid. In this limit, all particles will have their position-probability distributed equally throughout the fluid. Figure 1.2 shows the constant

value of $|\Psi|^2$ throughout the fluid.
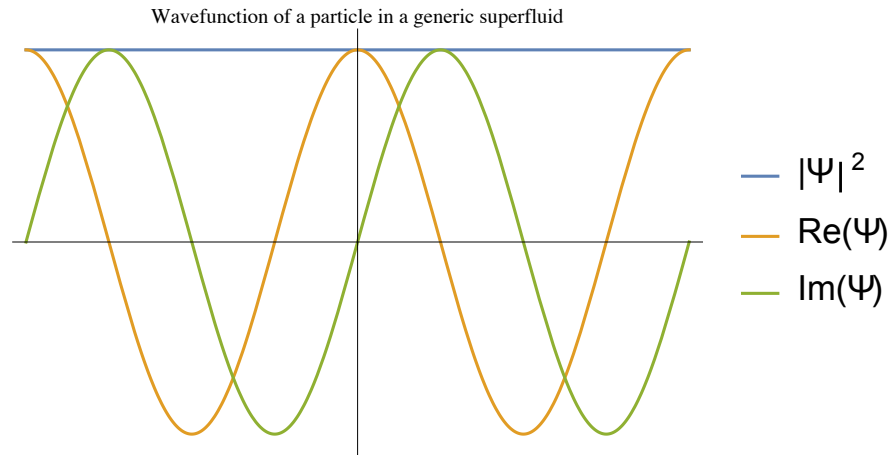
Figure 1.2: Each particle is distributed equally throughout the entire superfluid

This ground state wavefunction can be written in a position basis as

$$\Psi_0(\vec{r}) = \sqrt{\rho} \ e^{i\Phi(\vec{r})} \tag{2}$$

Where ρ is the density and $\Phi(\vec{r})$ is a quantum phase function.

Superfluids are incompressible, and as such, obey Laplace's equation for a flow phase ψ.

$$\nabla^2 \psi = 0 \tag{3}$$

Where the flow phase function is defined as the flow field's gradient

$$\vec{\nabla} \psi = \vec{v} \tag{4}$$

For superfluids, the quantum phase, Φ is actually equal to the flow phase,

ψ. Because the particles are all aligned in the same quantum configuration in the superfluid limit, there is no particle scattering, and therefore no viscous drag. However, in any real situation, there will be thermal fluctuations, and dissipation will occur.

The Quantum Fluids Group at Wesleyan has performed an experiment in which a superfluid film is driven to resonate in a third sound wave motion (essentially a sloshing back and forth in which the horizontal motion dominates and any vertical motion is negligible). [B., C., G., and H.] The driving would be turned off, and the decaying amplitude of the wave motion measured over time. If the decay were only from thermal fluctuations, we would observe an exponential amplitude decay, such as was observed in the cavity resonance chamber discussed in the Honor's Thesis of Swaminathan '09. On a log scale, these amplitude decays correspond to a straight line, as seen in Figure 1.3.
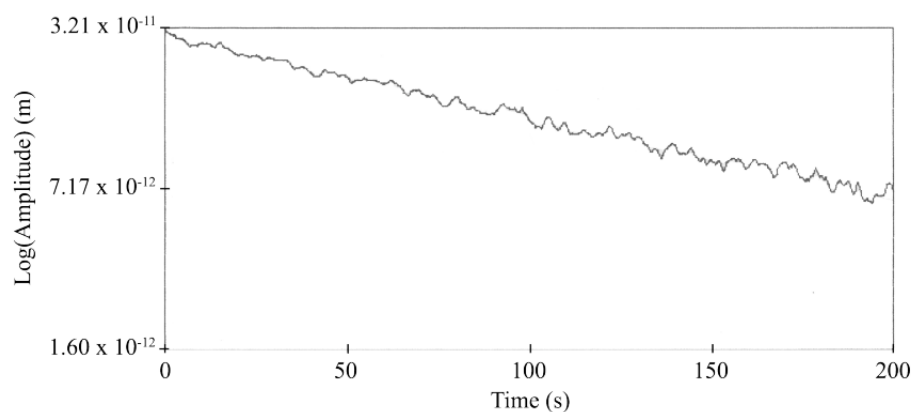
Figure 1.3: Third sound flow amplitude displaying exponential decay consistent with thermal fluctuations [B.]

However, Swaminathan also found many decays that displayed more anoma-lous behavior. Both "kink" and "bulge" functional patterns (as shown in Figure 1.4) were observed, in which the rate of decay was dependent on the amplitude of flow. This would suggest a mechanism beyond simple thermal fluctuations.

Figure 1.4: "bulge" dissipation behavior (above) and "kink" dissipation behavior (below) [B.]

One of the other possible causes of dissipation, in addition to thermal fluctu-

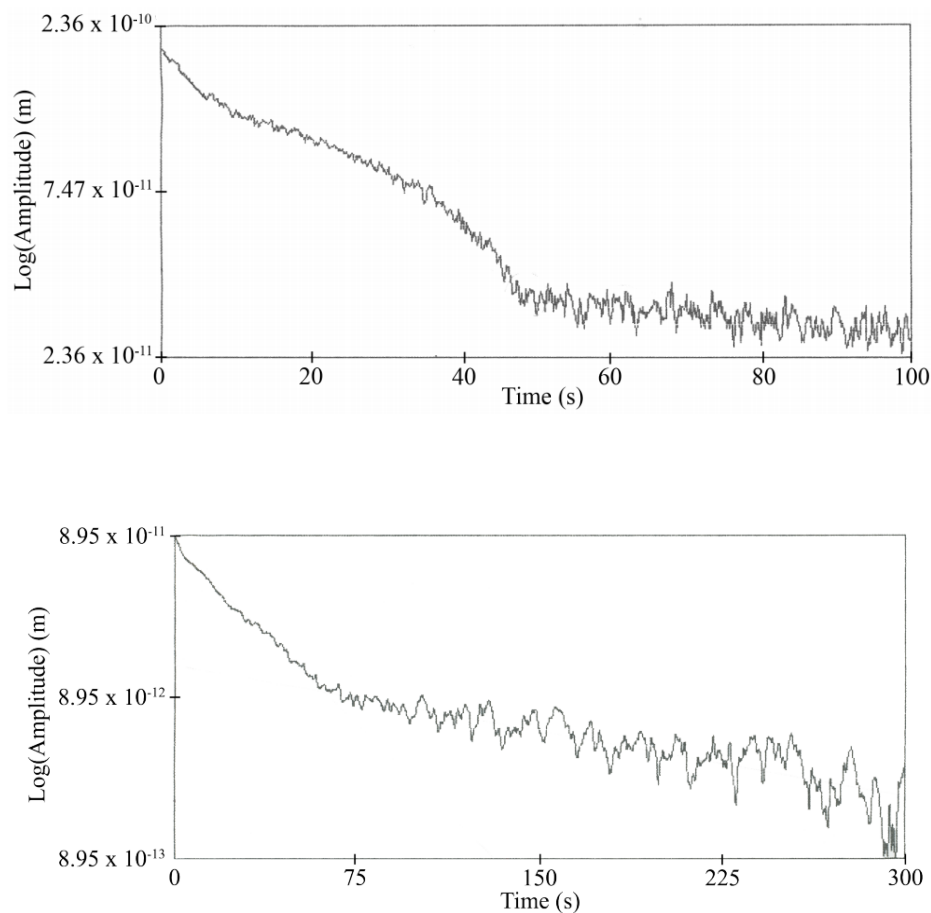ations, is the presence of superfluid quantum vortices. These behave exactly like normal fluid vortices, except for the fact that they can only exist on specific quantized levels.

A quantum vortex can be viewed as a quantized circular flow with closed streamlines around a vortex core. Each vortex is characterized by a circulation strength, K, defined as

$$K = \oint \vec{v} \cdot \overrightarrow{dl} = n \frac{\hbar}{m_4} \tag{5}$$

Where $\hbar$ is Planck's constant, m_4 is the mass of a single ^{4}He atom, and n represents the quantization level of the vortex. In a two-dimensional film, the velocity is given by

$$\vec{v} = n \frac{\hbar}{m_4 \, r} \hat{\phi} = \vec{\nabla} \psi \tag{6}$$

Where r is the radial distance from the vortex core line, and $\hat{\phi}$ represents the azimuthal direction (with the right hand rule). The flow phase function ψ, which also corresponds to the quantum phase function, can be found by solving Laplace's equation for the appropriate velocity gradient.

$$\psi(\vec{r}) = \psi_0 + \int_{\vec{R_0}}^{\vec{r}} \vec{v} \cdot \overrightarrow{dl} \tag{7}$$

Where $\vec{R_0}$ is an arbitrarily defined reference point, and ψ_0 is an arbitrary

constant. For a vortex on a 2D surface, we can define $\psi_0 = 0$ along a line of azimuthal angle 0 relative to the vortex core, and integrate in an arc around the core to get the phase (since the vortex's velocity will always be in the $\hat{\phi}$ direction).

$$\psi(\vec{r}) = \int_{\phi'=0}^{\phi'=\phi} \vec{v} \cdot \vec{dl} = n \, \frac{\hbar}{m_4} \, \phi \tag{8}$$

We will consider only vortices of the $n = 1$ case, as vortices with n'>1 tend to quickly decay into n' vortices at the energy level n=1. As we shall see, 2 n=1 vortices actually carry less energy together than 1 n=2 vortex, due to the quadratic relation between velocity and energy.

Energy of a fluid film is calculated via the equation

$$E = \frac{1}{2} \int v^2 \, dm = \frac{\rho h}{2} \int v^2 \, dA \tag{9}$$

Because of the first order reciprocal relation between vortex velocity and radius, an energy integral over all space for a single vortex does not converge. Therefore, we expect vortices to form in pairs of opposite circulation, so that their kinetic energy will come from a dipole flow nearby, but will cancel in the far flow limit.

Due to Bernoulli effects, vortices experience a Magnus force in the presence of a background flow. The vortex flow will create regions of high velocity where the vortex flow matches the direction of the background

flow, and by Bernoulli's Principle, these high velocity regions will have low pressure that drags the vortex in that direction.
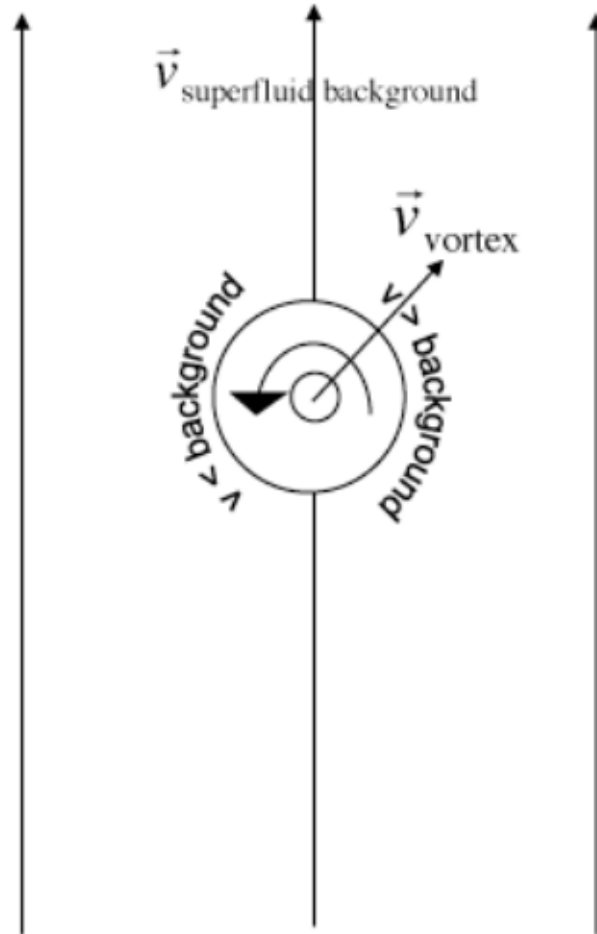

Figure 1.5: Magnus force effects on the vortex core.

This Magnus force can be calculated by the following equation:

$$\vec{F}_{\text{Magnus}} = \rho \kappa h \left(\vec{v}_{\text{vortex}} - \vec{v}_{\text{background flow}} \right) \times \hat{k} \tag{10}$$

The Magnus force will drag vortices apart if they are in the proper align-

ment - in figure 1.5, this would correspond to a positively quantized vortex (as shown) on the right and a negatively quantized vortex (not shown) on the left, by the right hand rule. Vortices are attracted together by a dipole attraction proportional to $\frac{1}{r^2}$ due to each vortex experiencing a Magnus force from the flow field of the other vortex. The pair will annihilate if their attraction is strong and they come together. However, at some point the background flow Magnus force overpowers the dipole attraction, and the vortices will continue to separate on their own, in a process known as nucleation. Examining conditions for nucleation will be an important part of this project.

Whereas vortices in normal fluid form gradually, with smaller eddies flowing back on themselves and creating larger eddies, quantum vortices in superfluid must instantaneously transition from an n = 0 state (no vortex) to an n = 1 state (fully formed vortex). Therefore, it is of great interest what types of conditions will lead to vortex pair formation in the superfluid. The results of the Quantum Fluids Group show that there was much higher dissipation from the Stimulated Condensation resonator (which has a visibly rough outer surface, indicating defects on the substrate) than there was from the cavity resonator, which had smooth epoxy walls on the corresponding surface. Some examples of surface defects on metallic substrates are shown in Figure 1.6.
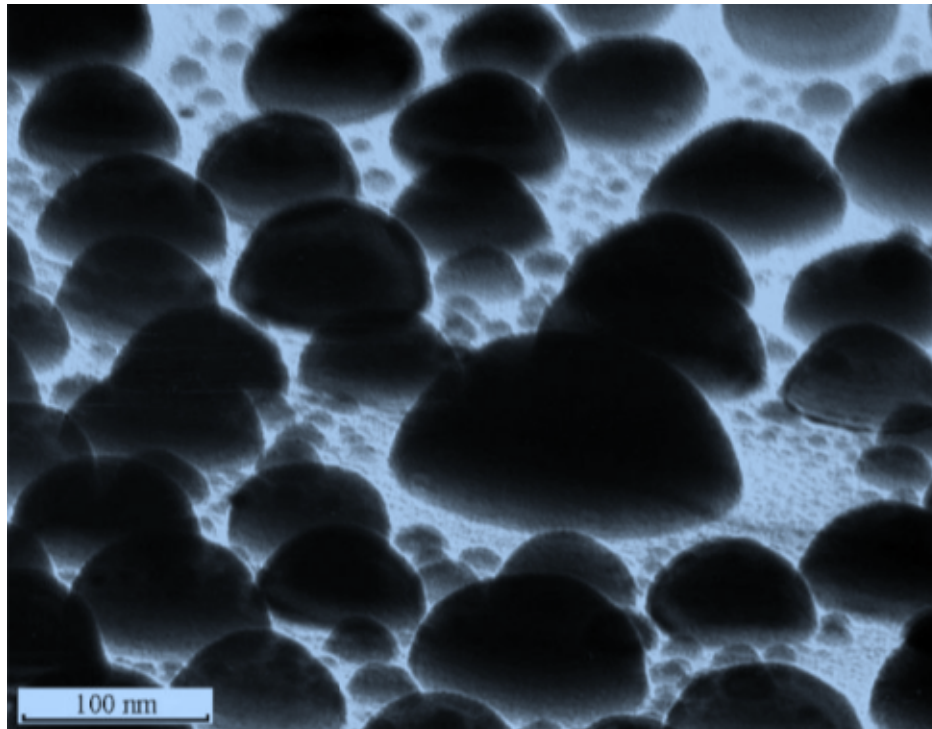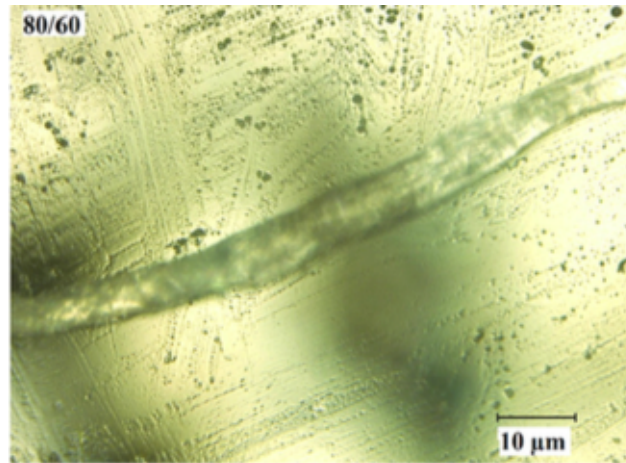
Figure 1.6: examples of surface defects on a metallic substrate. Silicon Dioxide (above) [D.] and evaporated Mercury on Gold [E.] (below)

With this project, we seek to determine what types of surface defects on the substrate could be conducive towards vortex formation. We will examine

the cases of a spherically symmetric bump and a complete obstruction to flow.

Image Solutions

The flow phase function given by (8) satisfies Laplace's equation and completely describes the flow from a vortex on an infinite 2-dimensional film. However, to model vortex flow around surface defects or constrictions to flow, we will need to be a little more creative in our solution to satisfy both Laplace's equation and Neumann boundary conditions (conditions on $\vec{\nabla}\psi$). Fortunately, we can use the uniqueness theorem for Laplace's equation, which says that if we know $\vec{\nabla}\psi$ on all the boundaries of a surface, any solution ψ that satisfies the boundary conditions and Laplace's equation will be correct and will have a unique gradient. Therefore, if we concoct specific ψ solutions that satisfy the conditions on its gradient, we will correctly define the unique flow field.

The method that we use to concoct these potential functions is the method of images. That is to say, we construct our solution to Laplace's equation by attempting to satisfy boundary conditions through the inclusion of fictitious vortices that exist in nonreal space. This is analogous to solving for electromagnetic potential through the use of image charges. Virtual vortex images need not be quantized, they can have any circulation strength that will appropriately match boundary conditions.

We can look at a simple example to demonstrate how this works. Imagine a

vortex core at some arbitrary position within a cylinder containing a superfluid film.
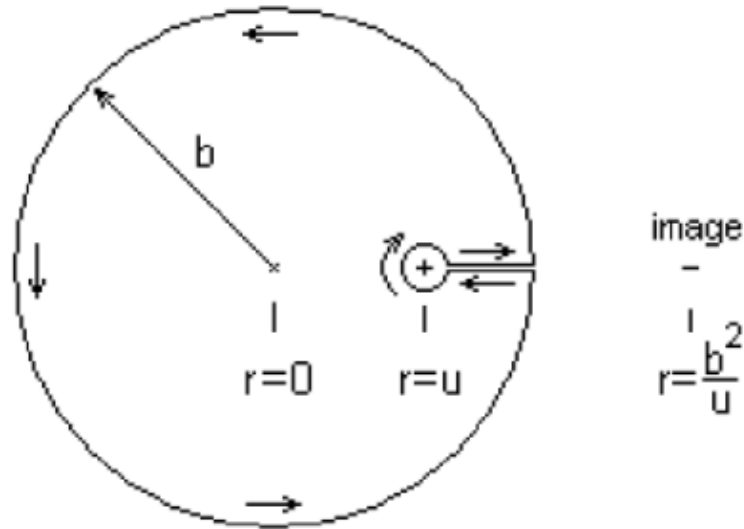
Figure 1.7: A vortex and it's image. The arrows represent an integration path for equation (14).

The boundary condition here is that there must be no flow through the boundary:

$$\vec{\nabla}\psi\,|_{r=b}\cdot\hat{r}\;=\;0 \tag{11}$$

The flow phase for an isolated vortex, as given by (8), would not satisfy this boundary condition. As such, we construct an image vortex outside of the cylinder to cancel radial flow at the boundary. Taking advantage of complex analysis, we can write our phase function in a different way that

will work out easier than the azimuthal function defined by (8).

$$\psi(x, y) \;=\; \mathrm{Re}\!\left(-i * \frac{\kappa}{2\,\pi} * \ln\!\left(\frac{z - z_{\mathrm{vortex}}}{a_0}\right)\right) \tag{12}$$

Where

$$z \;=\; x \;+\; i\mathrm{y} \tag{13}$$

and a_0 is the vortex core radius. This form of ψ will give us the same gradient function as (8), so we know that it must be correct by the Uniqueness Theorem. We then add the image vortex of opposite circulation at $\mathrm{x} = \frac{b^2}{u}$ (such that the geometric mean of the two vortex radii will be the radius of the cylinder) to cancel radial flow around the boundary. The vortex along with its image is shown in Figure 1.7. The full phase function is:

$$\psi(z) \;=\; \mathrm{Re}\!\left(-i * \frac{\kappa}{2\,\pi}\left(\ln\!\left(\frac{z - u}{a_0}\right) - \ln\!\left(\frac{z - \frac{b^2}{u}}{a_0}\right)\right)\right)$$

This phase function actually fulfills Laplace's equation and the Neumann boundary condition at the edge of the cylinder, and we are done solving for the flow field.

To calculate the energy of this vortex configuration, we can make use of Green's first identity to turn (9), a 3-dimensional mass-element integral which had been simplified into a 2 dimensional surface integral, into a 1-dimensional path integral. Green's first identity states for any volume inte-

gral with a differentiable ψ of the following form,

$$\int_V \left(\psi \, \nabla^2 \psi + \left(\overrightarrow{\nabla} \, \psi \right)^2 \right) dV = \oint \psi \left(\overrightarrow{\nabla} \, \psi \cdot \hat{n} \right) dS$$

Noting that $\nabla^2 \psi = 0$, the volume integral can be reduced to a path integral around the boundary of the enclosed volume, with $\hat{n}$ pointing outward from the enclosed volume. Our energy integral reduces to

$$E = \frac{\rho h}{2} \oint \psi \left(\overrightarrow{\nabla} \, \psi \cdot \hat{n} \right) dS \tag{14}$$

We want our path to go all the way around the boundary of the cylinder, with a match cut into the fluid to exclude the interior of the vortex core, which has a singular flow. This path is shown in Figure 1.7. The path around the edge of the cylinder will give a result of 0 due to the satisfied boundary condition that no flow be directed out of the cylindrical bounding surface. The path around the vortex core will also give 0, because we treat the core as a streamline. The only path that will give a contribution will be the match cut in and out between the vortex and the cylinder boundary. The velocities will be the same on the outward and inward path, and the phase of the image vortex will also be the same on the outward and inward path. The only contribution to the integral that will be different between them is the phase function of the real vortex - it will differ by the azimuthal angle of 2π accumulated by circulating around the vortex. $\psi_{\text{real vortex}} = \frac{K}{2}$ on the inward path and $\psi_{\text{real vortex}} = \frac{-K}{2}$ on the outward path. The velocity, found

from taking the gradient of our total ψ function, will be

$$\vec{v} = \vec{\nabla}\psi = \frac{K}{2\,\pi}\left(\frac{1}{x-u} - \frac{1}{x-\frac{b^2}{u}}\right)$$

The energy is then found by the following integral

$$E = 2 * \frac{1}{2}\rho h \int_{u+a_0}^{b} \frac{-K}{2}\left(\frac{-K}{2\,\pi}\left(\frac{1}{x-u} - \frac{1}{x-\frac{b^2}{u}}\right)\right) dx$$

Which evaluates to approximately

$$E = \frac{\rho h K^2}{4\,\pi}\ln\left(\frac{b}{a_0}\left(1 - \frac{u(u+a_0)}{b^2}\right)\right)$$

This approximate result holds for the situation that $b - (u + a_0) \gg a_0$, so that the kinetic energy of the fluid far from the singular vortex core dominates. We have defined the vortex core as being in the middle of the streamline; however, this is an approximation. When the vortex comes close to the boundary, the core may actually move off-center from the circular streamlines, but we choose not to consider these effects, which should be negligible so long as the vortex core is far from the boundary.

This example was done for a very simple case. We will now use these techniques to solve for vortex phase functions and energy integrals in more complicated, more realistic flow situations. While this single vortex inside the cylindrical shell does have a finite energy, a single vortex's kinetic energy goes infinite on an infinite flat plane of fluid. Therefore, single vortices are not likely to form by themselves on a real, semi-infinite flat

surface, so we will attempt to analyze vortex pairs instead.

Chapter 2: Obstruction to flow

Image Solutions

A complete obstruction to flow is actually a fairly simple case for finding a vortex solution to Laplace's equation. We have the same boundary condition (11) as we had for the case of the vortex in the cylinder - that radial flow through the obstruction boundary must be 0. The solution to Laplace's equation corresponding to a background flow diverted around a cylindrical obstruction is

$$\psi_{\mathrm{BF}}(z) = V_0\left(z + \frac{b^2}{z}\right) \tag{15}$$

Where V_0 is the background flow speed, b is the radius of the cylinder (centered at the origin), and z is the complex position representation defined by (13). The z term corresponds to the uniform background flow, and the $\frac{b^2}{z}$ term corresponds to a diversion of flow around the boundary. Figure 2.1 shows the flow field around the obstruction.
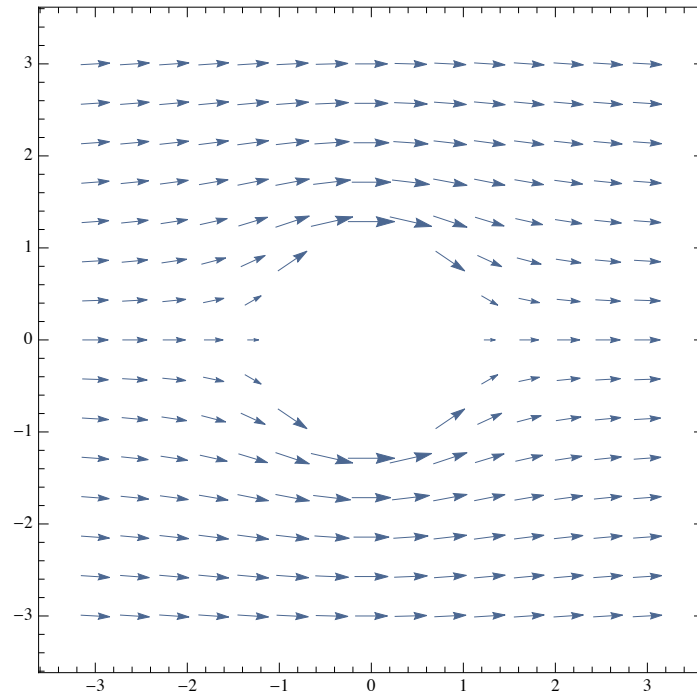
Figure 2.1: Background flow field around a cylindrical obstruction

The vortex image solution follows almost exactly from the analysis of the isolated vortex in the cylinder - except this time, we place the virtual image vortex inside the cylinder, with our real vortex outside of it - with the same condition that the geometric mean of the two vortex radii be the radius of the obstruction.

$$\psi_{\text{vortex}}(z) \;=\; \text{Re}\!\left(i * \frac{\kappa}{2\,\pi}\left(\ln\!\left(\frac{z-u}{a_0}\right) - \ln\!\left(\frac{z-\frac{b^2}{u}}{a_0}\right)\right)\right)$$

Figure 2.2 shows the flow field from the vortex with its image in the absence of any background flow.
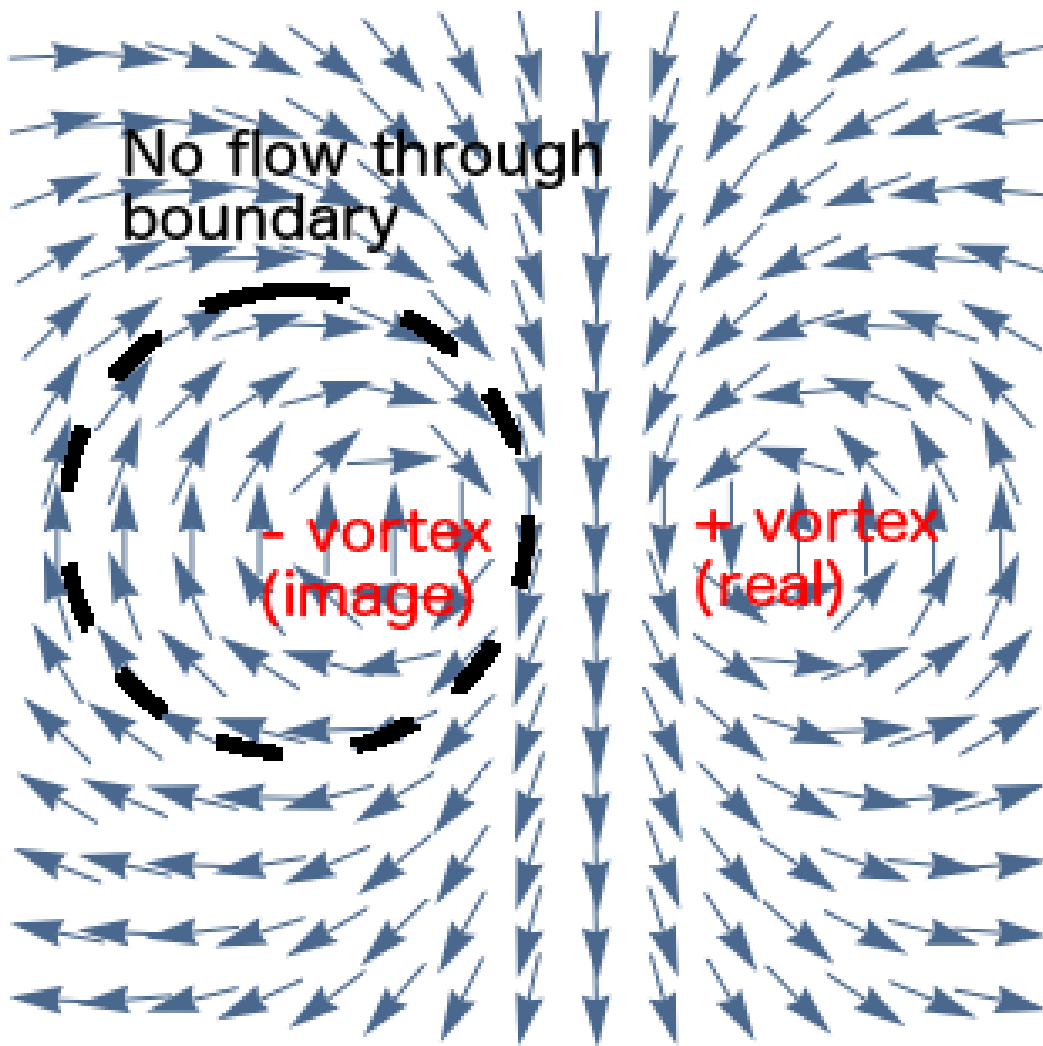
Figure 2.2: Vortex flow field around an obstruction with an appropriate image vortex inside.

With this mathematical framework, we want to figure out the energy difference between a static background flow versus a vortex pair in the background flow.

Calculating Energy

We consider a vortex pair arranged such that the Magnus force will pull

them apart - for a background flow in the positive x-direction, this corresponds to a negative vortex in the first quadrant and a positive vortex in the fourth quadrant. Using Green's first identity, we can use equation (14) to calculate energy as a line integral around the entire fluid. We will need to include all fluid out to infinity, but exclude the obstruction (which has no physical flow) and the vortex cores (which have a singular flow). This line integral can expressed as 4 separate paths, as shown on Figure 2.3:

(1): The circular path at r = ∞

(2): The circular path at r = b (around the obstruction)

(3): The circular path around the top vortex core

(4): The circular path around the bottom vortex core

(5): The vertical branch cut going to the top vortex

(6): The vertical branch cut going to the bottom vortex

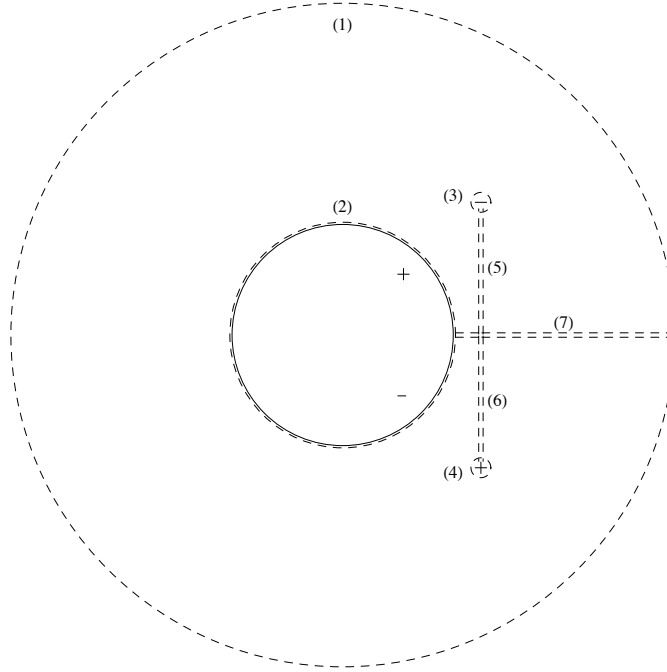(7): The horizontal branch cut between (1) and (2)

Figure 2.3: The dashed lines represent the path of integration. The "+" and "-" symbols refer to positively and negatively quantized vortices, respectively.

Paths (3) and (4) follow streamlines of the enclosed vortex, giving no contribution to the $\hat{n}$ direction of velocity. The change in ψ and $\vec{\nabla}\psi$ from the background flow and other vortices on this length scale is negligible, and these integrals will be approximately 0. Path (7) will always be 0, because the $\hat{n}$ component (pointing perpendicular to the background flow) of the two vortex flows perfectly cancel along that line, spaced evenly between them. Path (2) will also always be 0, because $\hat{n}$ points radially towards the obstruction, and we cannot have radial flow through the boundary of the obstruction. Paths (5) and (6) will each give the same result, by symmetry.

Path (1) will give us an infinite energy from the background flow, so we

want to calculate the energy difference between a configuration with a single pair of vortices, as shown in Figure 2.3, and a configuration with no vortices. For the configuration with no vortices, we no longer need to integrate along branch cuts to exclude vortex cores, but we will still need paths (1), (2), and (7), although (2) and (7) both evaluate to 0. Our total energy difference will be

$$\Delta E = E_{v1} + E_{v2} + E_{v3} + E_{v4} + E_{v5} + E_{v6} + E_{v7} - E_1 - E_2 - E_7$$

Where each E_{vi} represents the energy along path i with vortices, and each E_i represents the energy from path i with no vortices. Along path (1), the dipole vortex flow goes to 0, so the background flow will dominate and the integral will give the same result with and without vortices. Eliminating terms that cancel or evaluate to 0, we can calculate energy with

$$\Delta E = 2 E_{v5} \tag{16}$$

Path (5) has two parts: the path in, and the path back out. These two will have the same velocity and phase values, except that the phase of the encircled vortex changes by 2π between the paths going in and out. Summing together the background flow and individual vortex contributions, the flow phase is

$$\psi(z) = \mathrm{Re}\!\left(V_0\!\left(z + \frac{b^2}{z}\right) + i\,\frac{K}{2\pi}\,\ln\!\left(\frac{(z - z_v)\left(z - \frac{b^2}{z_v}\right)}{(z - z_v{}^*)\left(z - \frac{b^2}{z_v{}^*}\right)}\right)\right) \tag{17}$$

Where z_v is the position of one of the real vortices, and $z_v{}^*$ is its complex conjugate, the position of the other real vortex. Letting $(x_v, y_v) = (\mathrm{Re}(z_v),$ $\mathrm{Im}(z_v))$ and plugging this into (14), we evaluate the integral

$$\int_0^{y_v-a_0} \psi\left(\vec{\nabla}\,\psi\cdot\hat{n}\right)dS \;-\; \int_{y_v-a_0}^0 (\psi + 2\,\pi)\left(\vec{\nabla}\,\psi\cdot\hat{n}\right)dS$$

Which simplifies to

$$2\,\pi \int_0^{y_v-a_0} \left(\vec{\nabla}\,\psi\cdot\hat{n}\right)dS$$

This integral has an analytic result; the energy difference is therefore

$$\Delta\mathrm{E} \;=\; \rho\mathrm{hK}\Bigg(-V_0\bigg(y_v + \frac{b^2\,y_v}{x_v{}^2 + y_v{}^2}\bigg) -$$

$$\frac{K}{2\,\pi}\ln\Big(\Big(a_0\,\sqrt{\Big(b^4 + 2\,b^2\big(-x_v{}^2 + y_v{}^2\big) + \big(x_v{}^2 + y_v{}^2\big)^2\Big)}\Big)\Big/ \tag{18}$$

$$\Big(2\,y_v\big(-b^2 + x_v{}^2 + y_v{}^2\big)\Big)\Big)\Bigg)$$

Furthermore, we can scale our length and time units to massage this formula into a simpler form. Bearing in mind that $a_0 \simeq 1.3 * 10^{-10}\mathrm{m}$, let

$$r' = \frac{r}{a_0}$$

$$t' = \frac{K}{a_0{}^2} t$$

From this rescaling, it follows:

$$V_0{}' = \frac{a_0}{K} V_0$$

$$b' = \frac{b}{a_0}$$

$$x_v{}' = \frac{x_v}{a_0}$$

$$y_v{}' = \frac{y_v}{a_0}$$

This scales V_0 to the maximal fluid speed of the vortex near the core, which is also the speed of sound in liquid ^{4}He for a Mach number 1 system [F.]

This gives us

$$\Delta \mathrm{E} = \rho \mathrm{h} K^2 \left(-V_0{}' \left(y_v{}' + \frac{b'^2 \, y_v{}'}{x_v{}'^2 + y_v{}'^2} \right) - \right.$$

$$\frac{1}{2\pi} \ln\left(\left(\sqrt{\left(b'^4 + 2\, b'^2 \left(-x_v{}'^2 + y_v{}'^2 \right) + \left(x_v{}'^2 + y_v{}'^2 \right)^2 \right)} \right) \middle/ \right. \qquad (19)$$

$$\left. \left. \left(2\, y_v{}' \left(-b'^2 + x_v{}'^2 + y_v{}'^2 \right) \right) \right) \right)$$

We can also scale energy to Boltzmann's constant, which will give us

energy values in physically meaningful Kelvin units.

$$\frac{\Delta E}{K_B} = E' = T_0\left(-V_0'\left(y_v' + \frac{b'^2\, y_v'}{x_v'^2 + y_v'^2}\right) - \right.$$

$$\frac{1}{2\,\pi}\ln\left(\left(\sqrt{\left(b'^4 + 2\,b'^2\left(-x_v'^2 + y_v'^2\right) + \left(x_v'^2 + y_v'^2\right)^2\right)}\right)\Big/ \right. \tag{20}$$

$$\left.\left.\left(2\,y_v'\left(-b'^2 + x_v'^2 + y_v'^2\right)\right)\right)\right)$$

Where $T_0 = \frac{\rho h K^2}{K_B}$, which we can calculate numerically:

$$\rho = 145\,\frac{\text{kg}}{m^3}$$

$$h = 3*10^{-9}\, m$$

$$K = \frac{\hbar}{m_4} \simeq 1*10^{-7}$$

$$T_0 \simeq 313\, K$$

Equation (20) will have reflectional symmetry about the y-axis for x_v, as can be seen by x_v appearing only in even powers in the argument of the natural log. This reflectional symmetry can also be deduced from the fact that the integral along path (5) depends only on a difference in flow phase based on integrating around the vortex core (which can be taken as a constant outside the integral) and the flow phase gradient in the integrand.

Energy Landscapes

Using our analytic expression for energy, we can plot it as a function of vortex position. For $V_0 = .1 \frac{m}{s}$ and b = 100nm, a vortex pair moving away from the obstruction will move through the energy path shown in Figure 2.4.

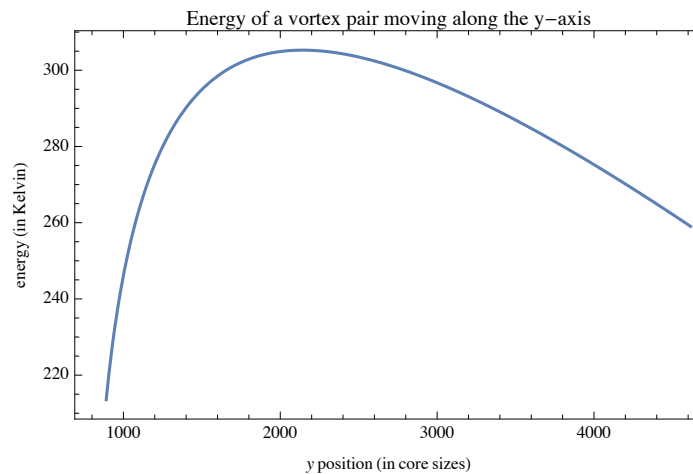Energy of a vortex pair moving along the y−axis

Figure 2.4: Energy path of a vortex pair separating along the y-axis.

The vortex pair moves to a higher energy configuration as it pulls away from the vortices' mutual dipole attraction, but after a certain energy barrier point, the energy starts to decrease in accordance with the background flow Magnus force winning out over the dipole attraction and working to pull the vortices apart.

We can make contour plots in which each point corresponds to the energy difference with a negative vortex on that point, and a corresponding positive vortex at a point reflected about the x-axis. For an obstruction of radius 100nm, we can look at the energy structure for different values of V_0. The

energy contour plots are shown in Figure 2.5, with the negative vortex positions plotted in the first quadrant. The second quadrant, corresponding to the vortex pair on the left side of the obstruction, will look exactly the same as the first quadrant mirrored about the y-axis. The third and fourth quadrants represent a vortex configuration in which the background Magnus force actually pushes the vortices together, and will not provide conditions favorable for nucleation.

$$V_0 = .32\frac{m}{s}$$
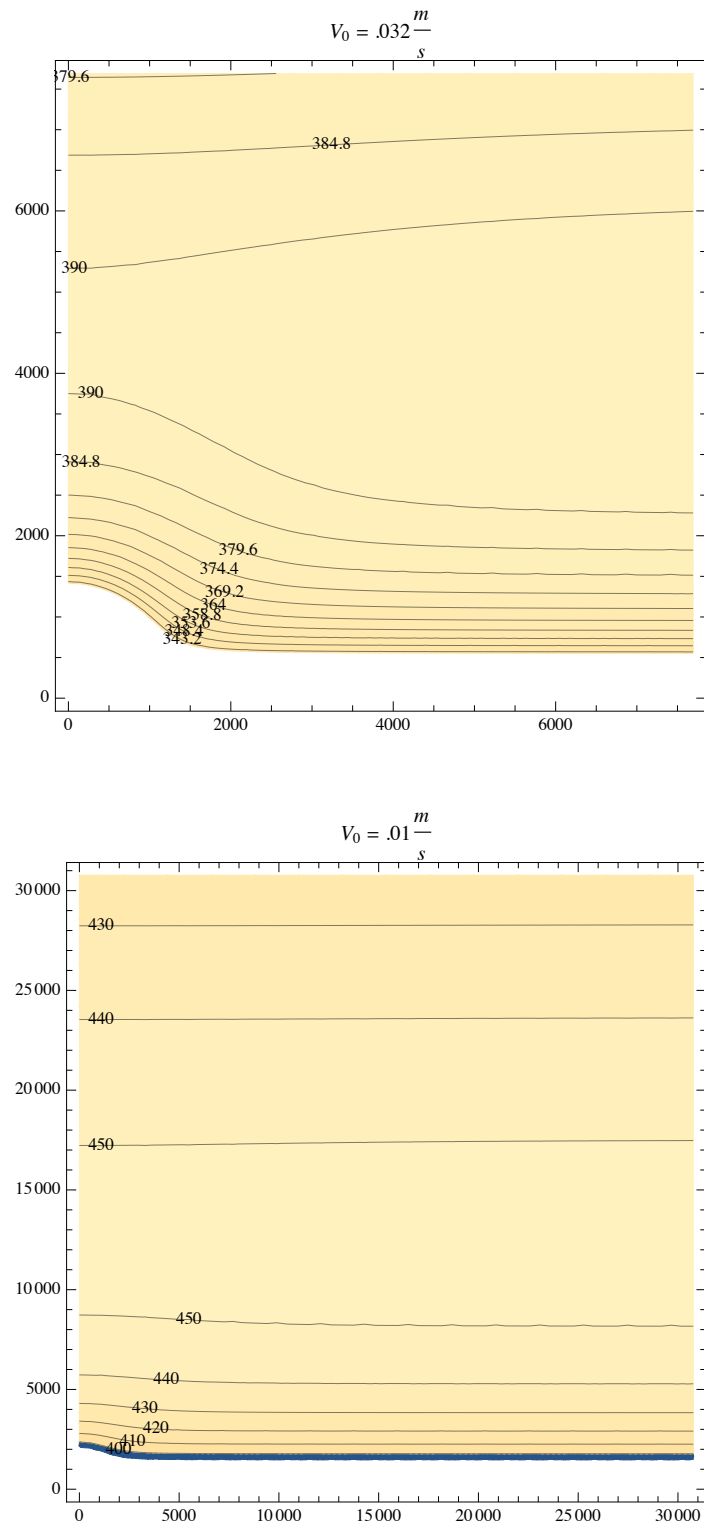

$$V_0 = .1\frac{m}{s}$$
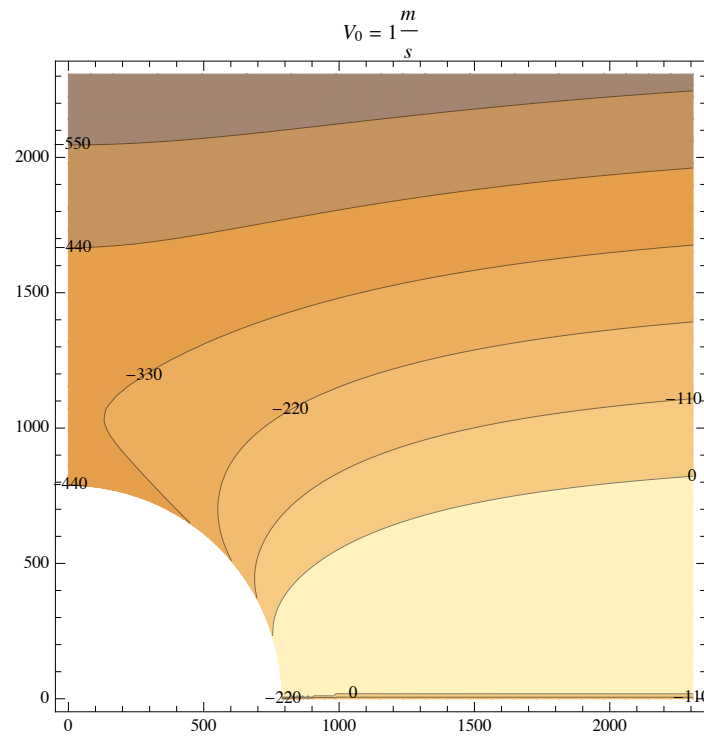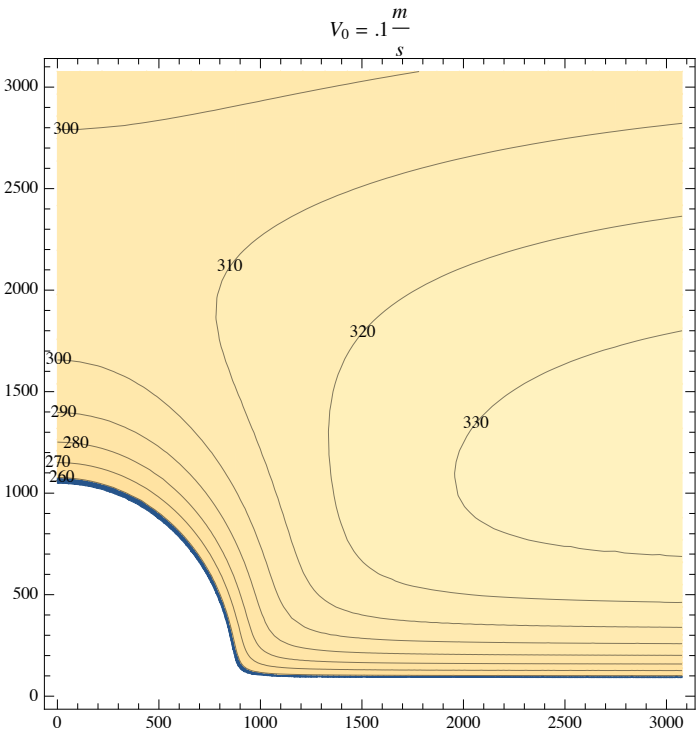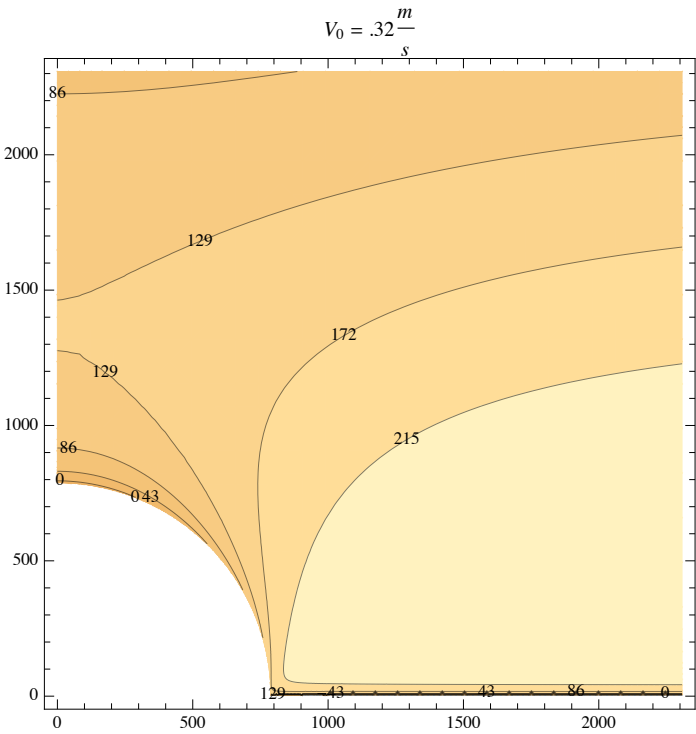
Figure 2.5: Contour plots of energy difference produced by a vortex pair. All energy units are in Kelvin, and all distance measurements are in units

of vortex core sizes.

Each plot has an appropriate range to observe the energy barrier above the obstruction. From these plots, two conclusions are immediately apparent: the energy barrier moves further away from the obstruction as background flow velocity goes down, and the energy barrier will have its lowest value along the y-axis.

Energy Barrier Analysis

Because we can graphically tell that the energy barrier will be the lowest along the y-axis, we can find the energy barrier by numerically finding the maximum energy point along the y-axis vortex trajectory.
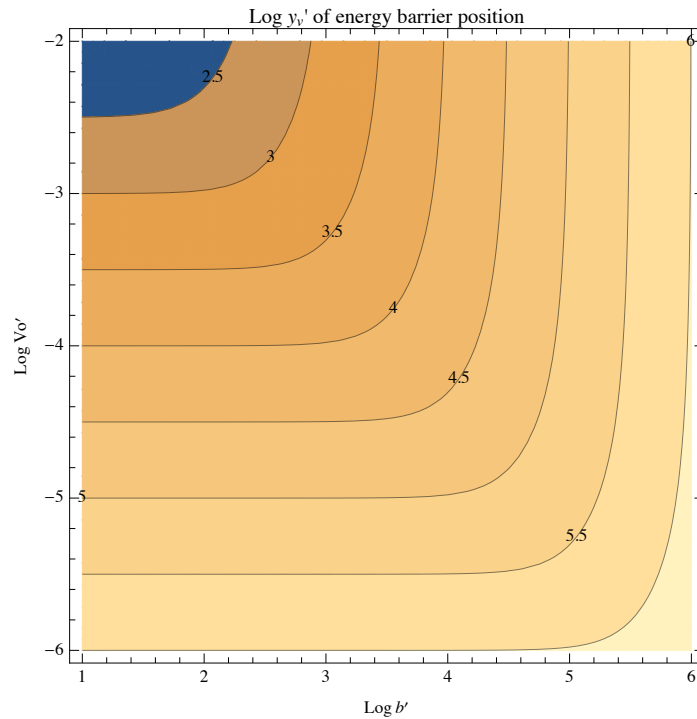

Figure 2.6: Log-log-log contour plot of energy barrier position as a func-

tion of scaled background flow velocity and obstruction size. b' $= \frac{b}{a_0}$ and

$$V_0' = \frac{a_0}{K} V_0$$

Figure 2.6 shows that the energy barrier seems to be closer to the obstruction for higher velocities and smaller obstruction sizes. It appears to vary linearly with both parameters. We can also contour plot the height of the energy barrier:
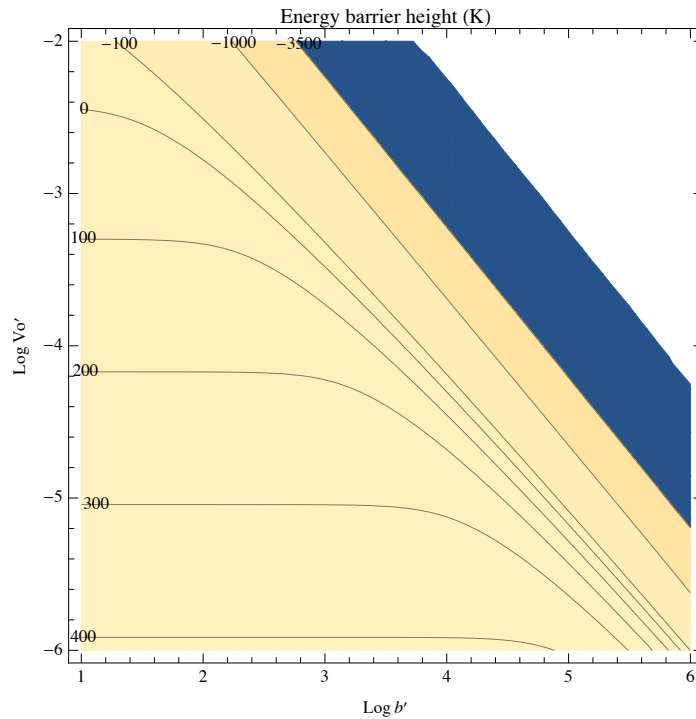

Figure 2.7: Log-log plot of the energy barrier height as a function of obstruction size and background flow velocity with the same scaling.

Figure 2.7 shows that the energy barrier is smaller for higher velocities and larger obstruction sizes. Therefore, a large velocity will create a closer, smaller energy barrier than a small velocity. A large obstruction size will

generate a smaller energy barrier, but the energy barrier position will be further away than for a smaller obstruction.

Now that we know about the energy landscape for a vortex pair around a cylindrical obstruction, we can compare it to the more realistic case of a vortex pair generated around a spherical bump that the superfluid can flow over.

Chapter 3: Spherical Bump

Film Thickness

We want to investigate flow and vortex behavior around and over spherical bumps, structures similar to those shown in the lower image of Figure 1.6. We consider a spherical bump characterized by a radial footprint a and a polar angle θ_b at which it meets the flat surface. This geometry is shown in Figure 3.1. Before investigating flow over the bump, we need to determine how the film thickness will change over the bump.
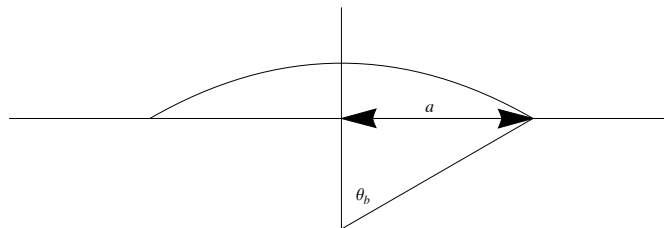

Figure 3.1: a spherical bump with radial footprint a and polar angle θ_b determining how much of the sphere is above the surface of the otherwise flat substrate.

We can calculate this roughly by equating the potential on the bump with

the potential on the flat at the boundary. On the flat, the potential comes from the Van der Waals interactions with the substrate, which acts like a local gravity. On the bump, there is again Van der Waals acting as local gravity attractor to the surface of the sphere, but there is also a surface tension term. Setting these potentials equal, we arrive at the following equation:

$$U_{\text{VDW}}(h_f) = U_{\text{VDW}}(h_b) + U_{\text{ST}}(h_b)$$

Where h_f is the film thickness on the flat, and h_b is the thickness on the bump. Plugging in expressions for Van der Waals and surface tension potential, we get

$$\frac{-\alpha}{h_f{}^3} = \frac{-\alpha}{h_b{}^3\left(1 + \frac{h_b}{2}\frac{\text{Sin}(\theta_b)}{a}\right)^3} + \frac{\gamma m_4}{\rho\left(\frac{a}{\text{Sin}(\theta_b)} + h_b\right)} \qquad (21)$$

ρ is the density of liquid helium $(145 \frac{\text{kg}}{m^3})$, m_4 is the mass of the helium nucleus, $(6.646 * 10^{-27} \text{ kg})$, α is the Van der Waals constant $(2.19865 * 10^{-50} \text{ Jm})$, and γ is the surface tension constant $(3.7 * 10^{-4} \frac{J}{m^2})$. By multiplying both sides of equation (21) by all of its denominators, we get a 7th degree polynomial of h_b with no analytic solutions. However, we can numerically find these roots. It turns out that for any positive, real values of a and θ_b, there is only one real positive root, and that is our desired solution. The ratio of bump to flat film thickness for a 100nm bump with a 3nm film on the flat is plotted as a function of θ_b in Figure 3.2.
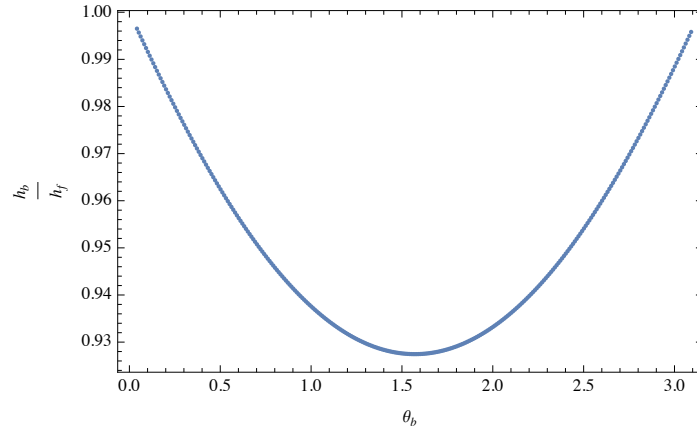
Figure 3.2: Ratio of bump film thickness to flat film thickness as a function of θ_b for a 100nm footprint bump with a flat film of 3nm.

Note that this analysis assumes a constant film height on the bump, which will not necessarily be accurate, as surface tension will cause the film to deform around the boundary to reduce surface area. Our calculations for film height are probably an accurate ballpark, though.

Image Solutions

The boundary conditions for a bump are more complicated than those for an obstruction: the volume flow perpendicular to the boundary must match on the flat and bump, and the flow velocity parallel to the boundary must match on the flat and bump.

$$h_b \, \vec{\nabla} \psi_b \cdot \hat{\theta} \; = \; h_f \, \vec{\nabla} \psi_f \cdot \hat{r} \tag{22}$$

$$\vec{\nabla} \psi_b \cdot \hat{\phi} \; = \; \vec{\nabla} \psi_f \cdot \hat{\phi} \tag{23}$$

Using these boundary conditions, as well as the condition that $\vec{\nabla} \psi_f$ go to

$V_0\,\hat{x}$ for large r, we can solve Laplace's equation for our background flow phase functions:

$$\psi_f(r,\phi) \;=\; V_0\!\left(r + \frac{a^2(h_f - h_s)}{h_f + h_s}\,r^{-1}\right)\mathrm{Cos}(\phi)$$

$$\psi_b(\theta,\phi) \;=\; \frac{2\,V_0}{1 + \frac{h_b}{h_f}}\,\frac{\mathrm{Tan}\!\left(\frac{\theta}{2}\right)}{\mathrm{Tan}\!\left(\frac{\theta_b}{2}\right)}\,\mathrm{Cos}(\phi)$$

On the flat, the background flow phase around the bump reduces to the unobstructed background flow phase in the limit that the film heights are equal on the flat and bump surfaces. The bump flow phase actually corresponds to a dipole-type of flow, but we place the dipole structure on the underside of the bump, and the rest of the function's gradient matches the flat velocity according to our boundary conditions. The bump phase is plotted on the surface of a 3D sphere in Figure 3.3.
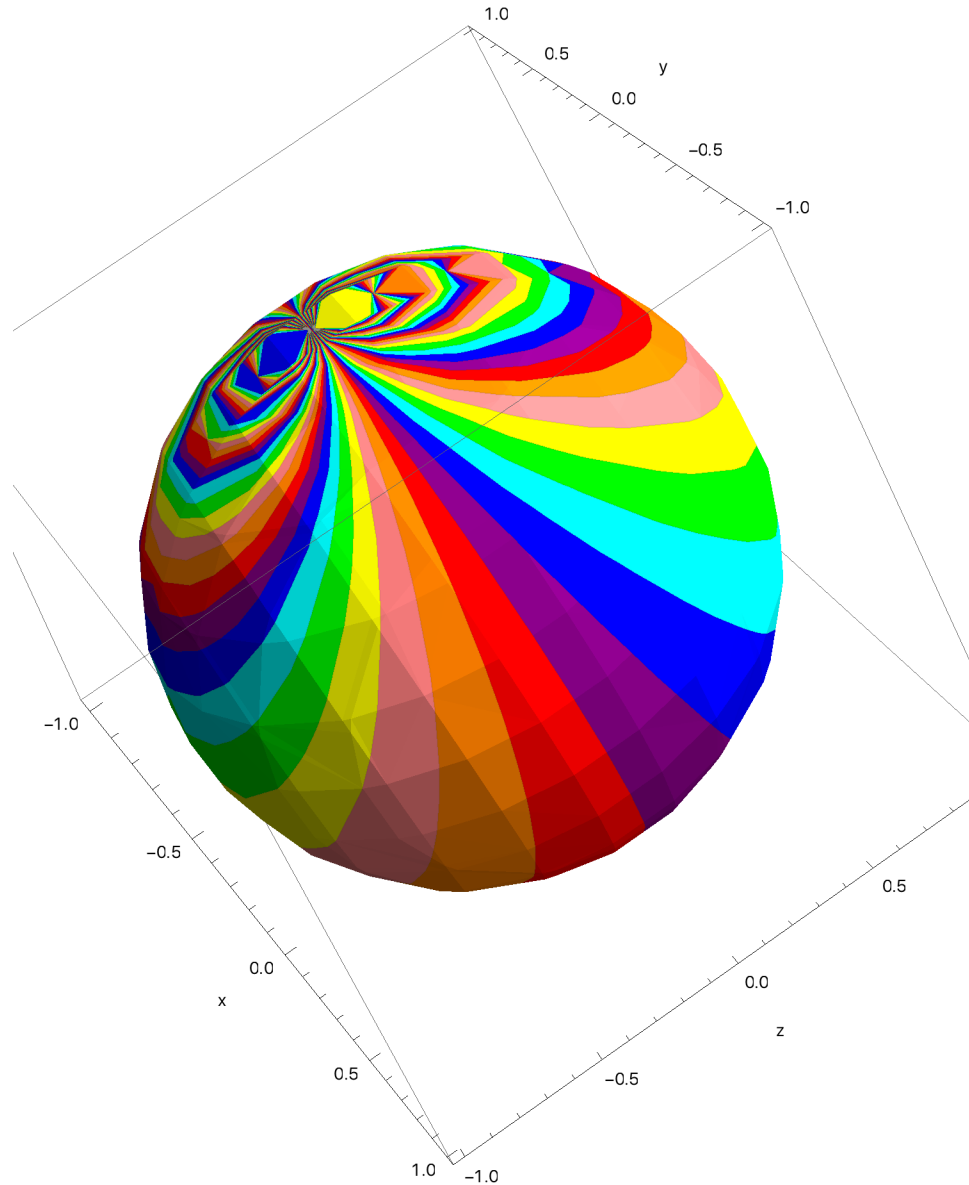
Figure 3.3: The background flow phase on the sphere. The dipole-like structure, shown on top, is placed on the underside of the bump so that it does not influence flow in real space.

Solving for the flow phase of a vortex is more difficult, because we cannot simply construct it from separable solutions to Laplace's equation. We can calculate the flow phase from equation (7) by taking a line integral of veloc-

ity from an arbitrarily defined reference point. We can find the velocity field with the Biot-Savart Law, (equation (24) keeping in mind that a vortex's flow field is analogous to a current-carrying wire's B-field.

$$\vec{v}(\vec{r}) \;=\; \frac{K}{4\,\pi} \int\limits_{\text{Vortex Line}} \frac{\vec{r'} \times \hat{t}}{(r')^3}\, ds \tag{24}$$

In 3D, this integral evaluates to an analytic result for the flow from a vortex line.

We consider a vortex line coming into the origin from the -x, +z direction, and leaving the origin from in +x, +z direction, both at polar angle β from the z-axis. This vortex "V" is shown in Figure 3.4.
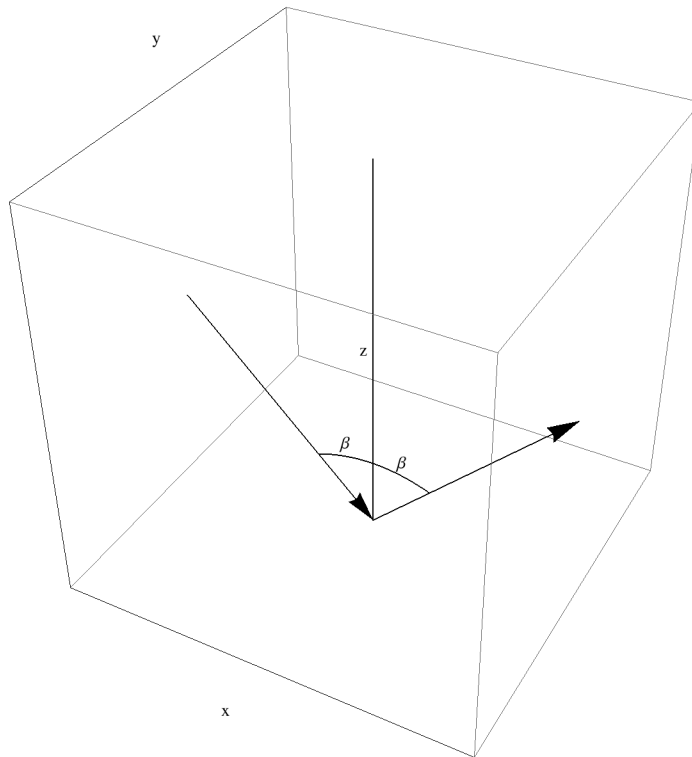

Figure 3.4: The vortex "V" in the X-Z plane at polar angle β. The direction

of the arrows represents the direction of vorticity.

Then the Biot-Savart integral through the vortex line gives us the following result:

$$\vec{v}(\beta, x, y, z) = \frac{K}{4\,\pi r} \frac{1}{r^2 - x^2 - 2\,rz\text{Cos}(\beta) + \text{Cos}^2(\beta)\left(x^2 + z^2\right)} \ * \tag{25}$$

$$\begin{pmatrix} -\text{Sin}(2\,\beta)\,xy \\ \text{Sin}(2\,\beta)\left(x^2 + z^2\right) - 2\,r\text{Sin}(\beta)\,z \\ y(2\,r\text{Sin}(\beta) - z\text{Sin}(2\,\beta)) \end{pmatrix}$$

Where $r = \sqrt{x^2 + y^2 + z^2}$. By symmetry, this flow is parallel to any spherical surface, so it is a valid flow for a film on an actual spherical surface. To find the flow phase, we set it's 0 point to be at x=0, z = -∞, along a line parallel to the y-axis. ψ will not change with movement along the y-direction, due to the contributions from the positive and negative vortices canceling by symmetry. From a point $\begin{pmatrix} 0 \\ y \\ -\infty \end{pmatrix}$ we integrate to $\begin{pmatrix} 0 \\ y \\ z \end{pmatrix}$ in the z-direction, and then add a path integral from $\begin{pmatrix} 0 \\ y \\ z \end{pmatrix}$ to $\begin{pmatrix} x \\ y \\ z \end{pmatrix}$ in the x-direction.

$$\psi(\beta, x, y, z) = \int_{-\infty}^{z} v_z(0, y, z')\,dz' + \int_{0}^{x} v_x(x', y, z)\,dx' \tag{26}$$

These integrals evaluate to the analytic, but very cumbersome, solution:

$$\psi_{\text{vortex on sphere}}(\beta, x, y, z) =$$

$$\frac{\frac{y}{|y|}}{2\pi}\left(\mathrm{ArcTan}\left[\frac{\mathrm{Cos}(\beta)\sqrt{1+\left(\frac{z}{|y|}\right)^2}-\frac{z}{|y|}}{\mathrm{Sin}(\beta)}\right]-\mathrm{ArcTan}\left[\right.\right.$$

$$\left.\left.\frac{\mathrm{Cos}(\beta)\sqrt{1+\left(\frac{x}{|y|}\right)^2+\left(\frac{z}{|y|}\right)^2}-\frac{z}{|y|}}{\mathrm{Sin}(\beta)}\right]\right)+$$

$$\arg\left(1+\frac{1}{4}\left(\sqrt{1+\left(\frac{z}{|y|}\right)^2}\,\mathrm{Tan}(\beta)-\frac{1}{\sqrt{1+\left(\frac{z}{|y|}\right)^2}}\,\mathrm{Cot}(\beta)\right)\right.$$

$$\left.\left(\frac{|y|}{z}\,\mathrm{Sec}(\beta)-\frac{z}{|y|}\,\mathrm{Sin}(\beta)\right)+\right.$$

$$\frac{i}{2}\left(\sqrt{1+\left(\frac{z}{|y|}\right)^2}\,\mathrm{Tan}(\beta)-\frac{1}{\sqrt{1+\left(\frac{z}{|y|}\right)^2}}\,\mathrm{Cot}(\beta)-\right.$$

$$\left.\left.\frac{|y|}{z}\,\mathrm{Sec}(\beta)-\frac{z}{|y|}\,\mathrm{Sin}(\beta)\right)+\mathrm{X}(z)\right)$$

Where X is the step function

$$X = \begin{cases} \frac{\pi}{2} & z > 0 \\ 0 & z \le 0 \end{cases} \qquad (28)$$

This solution features a discontinuity in the "V" formed by the vortex lines. Because the flow phase is not uniquely defined (only its gradient is unique), we can alternately define ψ with its 0 point in the "V" planar section. This alternate solution, which I'll call $\psi_{\text{vortex through}}$, works out amazingly similarly to the first solution:

$$\psi_{\text{vortex through}}(\beta, x, y, z) = \psi_{\text{vortex on sphere}}(\beta, x, y, z) - \frac{K}{2}$$

This solution once again has a discontinuity on the plane containing the vortex "V" but only on the section of the plane outside of the "V". We can redefine $\psi_{\text{vortex on sphere}}$ to include both solutions by giving another parameter, c, which can be either 1 or 0. c=0 corresponds to the solution with a discontinuity in the inner section of the "V" plane, c=1 corresponds to the solution with a discontinuity in the outer section of the "V" plane. The two types of solutions are shown pictorially from a top down perspective over the "V" in Figure 3.5.

$$\psi_{\text{vortex on sphere}}(\beta, x, y, z, c) =$$

$$\frac{\frac{y}{|y|}}{2\pi} \left(\text{ArcTan}\left(\frac{\text{Cos}(\beta)\sqrt{1 + \left(\frac{z}{|y|}\right)^2} - \frac{z}{|y|}}{\text{Sin}(\beta)} \right) - \right.$$

$$\text{ArcTan}\left(\frac{\text{Cos}(\beta)\sqrt{1+\left(\frac{x}{|y|}\right)^2+\left(\frac{z}{|y|}\right)^2}-\frac{z}{|y|}}{\text{Sin}(\beta)}\right)\right) +$$

$$\arg\left(1+\frac{1}{4}\left(\sqrt{1+\left(\frac{z}{|y|}\right)^2}\,\text{Tan}(\beta)-\frac{1}{\sqrt{1+\left(\frac{z}{|y|}\right)^2}}\,\text{Cot}(\beta)\right)\right.$$

$$\left(\frac{|y|}{z}\,\text{Sec}(\beta)-\frac{z}{|y|}\,\text{Sin}(\beta)\right)+$$

$$\frac{i}{2}\left(\sqrt{1+\left(\frac{z}{|y|}\right)^2}\,\text{Tan}(\beta)-\frac{1}{\sqrt{1+\left(\frac{z}{|y|}\right)^2}}\,\text{Cot}(\beta)-\right.$$

$$\left.\left.\frac{|y|}{z}\,\text{Sec}(\beta)-\frac{z}{|y|}\,\text{Sin}(\beta)\right)+X(z)-c\pi\right)$$

Figure 3.5: The two vortex pair flow phases, with their respective discontin-

uous branch cuts shown in bold. This picture is looking at the "V" cutting

through a sphere from a top-down perspective. The positive and negative

parts of the vortex line meet further down in the z-direction, at the origin.

We also need to match boundary conditions (22) and (23) for a vortex flow. This turns out to be a bit of a complicated mess, requiring multiple images in the flat and bump coordinate scheme. For the bump, we can place images on the underside of the bump, beneath the substrate (which does not exist in real space). For the flat, we can place images in the portions of the plane covered by the bump (which also does not exist in real space). We will need images in these regions whether the real vortex pair is on the surface of the bump or the flat. The series of images that match the boundary conditions are shown in Figure 3.6.
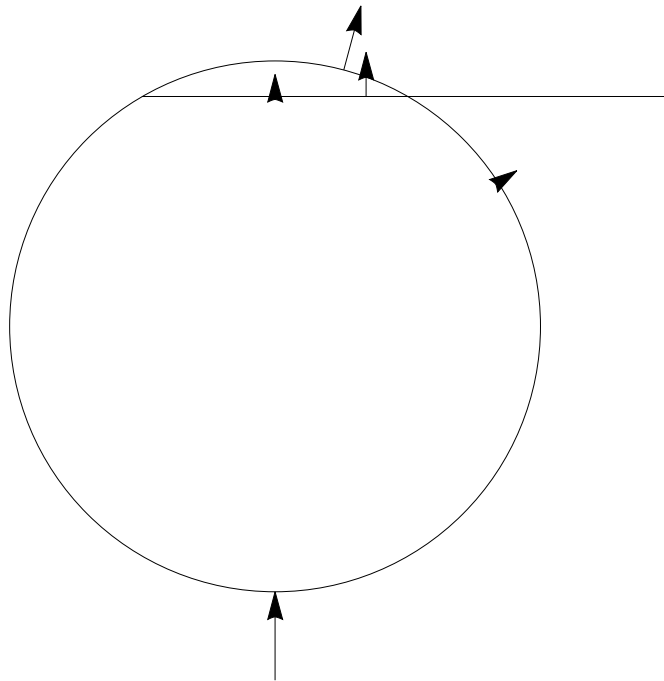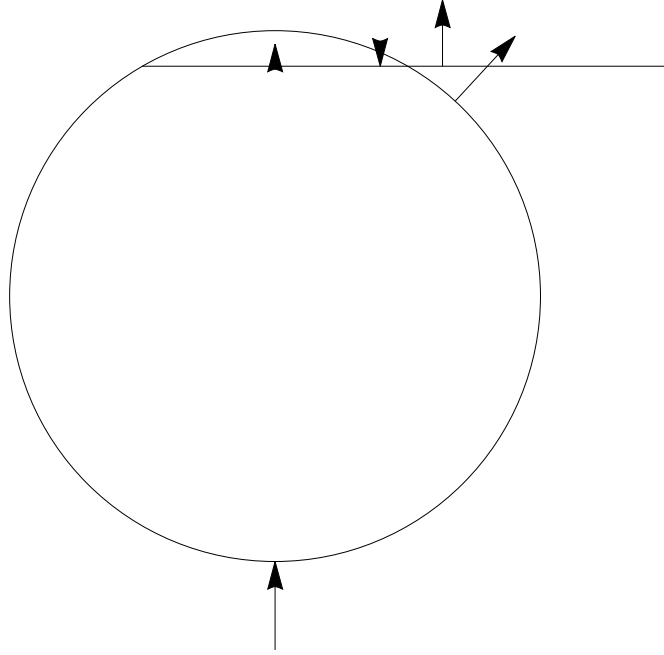
Figure 3.6: Pictures of the vortex images needed to match boundary conditions for a real vortex on the bump (above) and a real vortex on the flat (below). The arrow heights are scaled to the circulation strength of each vortex. h_s is set to $\frac{h_f}{2}$ for visual clarity.

For the vortex on the bump case, we have the following image vortices:

(1): The image on the sphere at $\theta = \pi$ with K' $= \frac{-2}{\frac{h_s}{h_f}+1}$

(2): The image on the sphere at θ_{si} with K' $= \frac{2}{\frac{h_s}{h_f}+1} - 1$

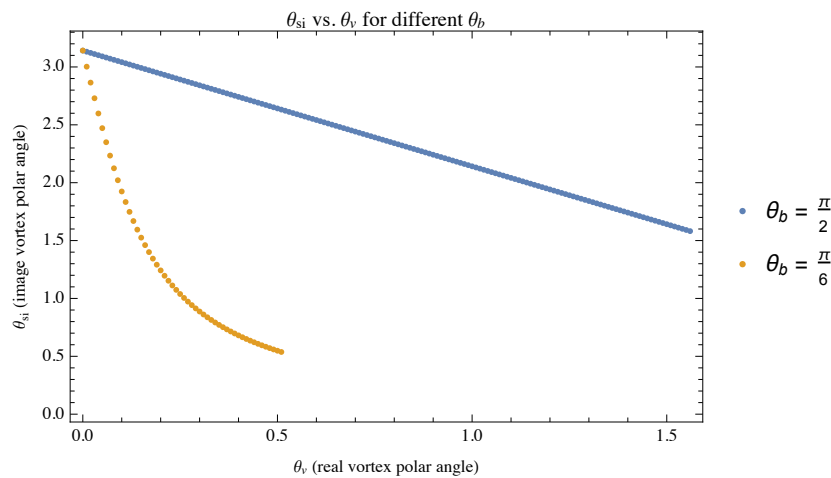(3): The image on the flat at r $= 0$ with K' $= \frac{2}{\frac{h_s}{h_f}+1} - 1$

(4): The image on the flat at r $= r_{fi}$ with K' $= 2 - \frac{2}{\frac{h_s}{h_f}+1}$

Where K' = $\frac{K_{\text{image}}}{K_{\text{real}}}$. θ_{si} and r_{fi} must be computed via numeric error minimization routines with regards to azimuthal flow velocity and radial volume flow error associated with boundary conditions (22) and (23). For the special case of $\theta_b = \frac{\pi}{2}$, they can be analytically calculated by

$$\theta_{\text{si}} = \pi - \theta_v$$

$$r_{\text{fi}} = \text{Cot}\left(\frac{\pi - \theta_v}{2}\right)$$

Where θ_v is the polar angle of the real vortex. Some sample values of θ_{si} and r_{fi} as a function of θ_v are shown in Figure 3.7 for different θ_b values. This configuration of images gives a net circulation of K in the flat coordinate scheme, which corresponds to the circulation K of the real vortex. There is a net circulation of -K on the underside of the sphere, which corresponds to a complete vortex line going through the sphere.
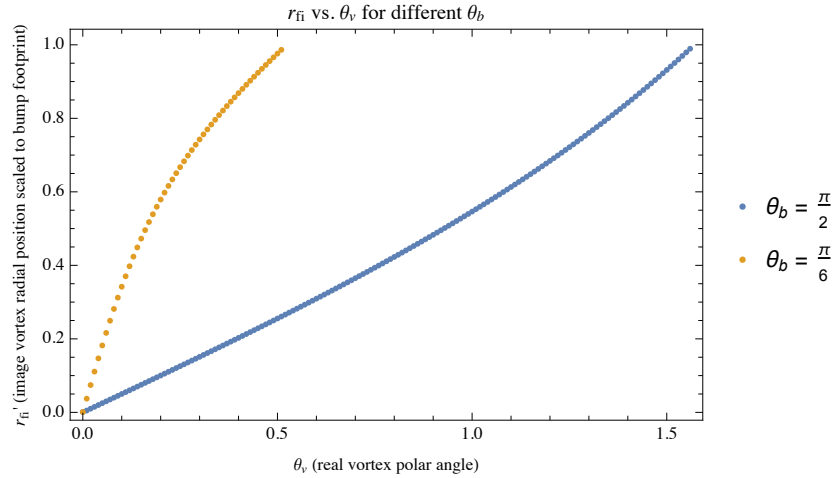
r_{fi} vs. θ_v for different θ_b

Figure 3.7: numerically computed values of θ_{si} (above) and r_{fi} (below) as a function of θ_v for two different values of θ_b.

For the vortex on the flat case, we have the following 4 images:

(1): The image on the sphere at $\theta = \pi$ with K' $= \frac{-2}{\frac{h_s}{h_f}+1}$

(2): The image on the sphere at θ_{si} with K' $= \frac{2}{\frac{h_s}{h_f}+1}$

(3): The image on the flat at r $= 0$ with K' $= \frac{2}{\frac{h_s}{h_f}+1}-1$

(4): The image on the flat at r $= \frac{1}{r_v}$ with K' $= 1 - \frac{2}{\frac{h_s}{h_f}+1}$

Where r_v is the flat radial distance of the real vortex from the axis of the bump perpendicular to the flat plane. θ_{si} must again be calculated by numeric minimization routine of boundary matching error. Some sample values are shown in Figure 3.8. In this image configuration, the two images

on the sphere have equal and opposite circulation, as do the two images on the flat. As such, there is no net vorticity other than the real vortex.
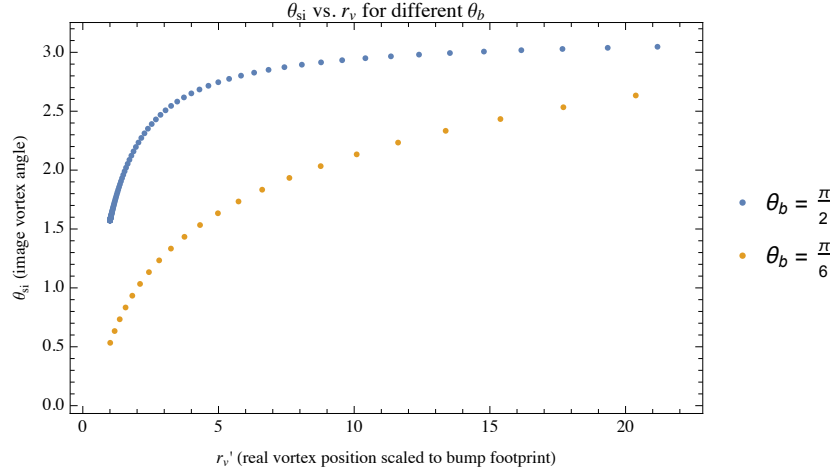

Figure 3.8: numerically computed values of θ_{si} as a function of θ_v for two different values of θ_b.

With this class of solutions, we have reduced boundary matching error to order of magnitude 10^{-16} for both boundary conditions in most situations. This indicates that our solutions are precise to the level of machine precision used for our program's internal computations, which would mean that there is probably an analytic solution for these images, although we were unable to find its exact form with our analytic methods. Also, error grows rapidly if we allow the real vortex to move within a core size of the boundary; we will not try to investigate such situations, because that would require treating the vortex core as a more nuanced structure that can be off-center from the circular streamlines.

When the real vortex moves from the bump to the flat, image (4) loses K

worth of circulation, and image (2) gains K worth of circulation. This corresponds to the sphere shedding its net vorticity and the flat images transitioning away from needing to represent the real vortex's flow on the flat.

Calculating Energy

Using equation (14) to calculate energy, we need two separate integration procedures - one for the case of a vortex pair on the flat, and one for the case of a vortex pair on the bump.

For the case of the vortex on the flat, the integration is actually not that complicated; to calculate the energy difference from the flow in the flat plane, we can repeat the exact same procedure we used to calculate the energy for a vortex pair around an obstruction (shown in Figure 2.3), except this time path (2) going around the bump will not necessarily be 0. We also need to calculate the kinetic energy difference from the flow on the bump, which means integrating again around the bump but in the bump coordinate scheme, with $\hat{n}$ pointing away from the fluid, parallel to the line tangent to the the bump's surface. I'll call the energy from this path E_{bump}. The energy we must calculate then is

$$\Delta E = E_{v2} + 2\, E_{v5} + E_{v\, \text{bump}} - E_2 - E_{\text{bump}} \qquad (30)$$

Where the $E_i's$ correspond to the ith path in Figure 2.3 and the subscript v corresponds to the configuration with a vortex. The quantity is well defined numerically and can be calculated, but it does not reduce to an analytic

solution.

For the case of a vortex pair on the bump, all the paths will be the same as they were for the vortex pair on the flat, except that the branch cut that was path (5) on the flat now must now be on the surface of the sphere, and path (7) will extend up the sphere surface in the X-Z plane. Path (7) will still evaluate to 0, because the vortex pair flow cancels along that line. Path (5) can be defined as the curvilinear intersection of the vortex pair "V" plane (characterized by an angle α) with the surface of the sphere. The path is shown as the line connecting the two vortices in Figure 3.9. α can be calculated by finding the polar angle of the average of Cartesian vectors pointing along the real vortex cores.
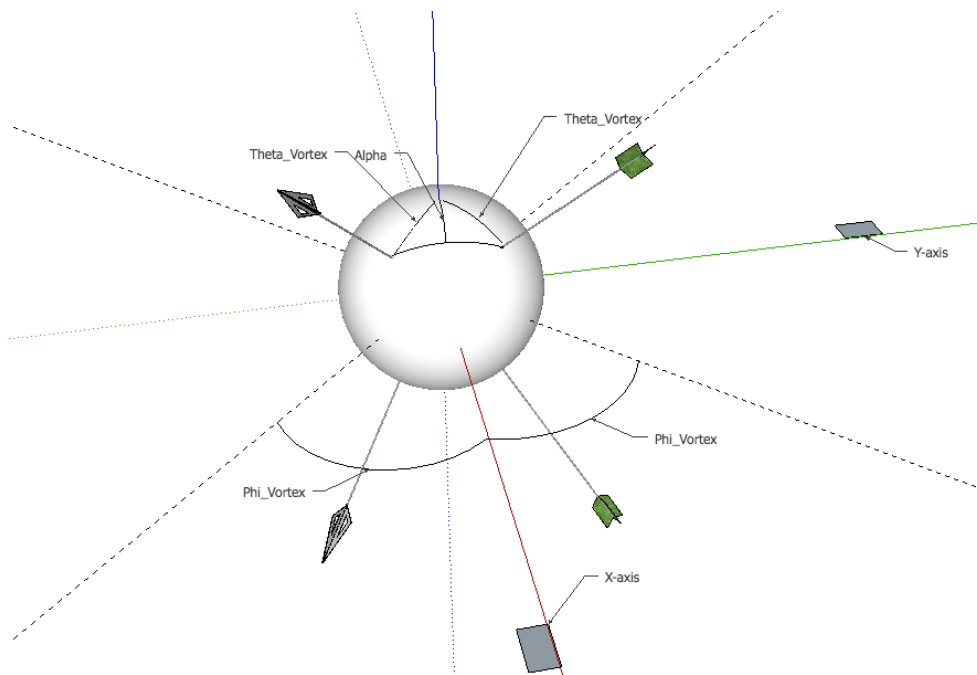

Figure 3.9: A representation of a real vortex pair on the topside of a sphere, with their images on the underside. The line connecting the real vortex pair is the intersection of the sphere surface and a plane of polar angle α.

So, if the vortex pair is on the bump, we can still use equation (30) to compute the energy difference associated with it, with the caveat that path (5) follow the more complicated curvilinear path shown in Figure 3.9.

We can also scale our distance and time measurements like we did for the case of the obstruction. Whereas we scaled distance to vortex core sizes for the obstruction, a more natural lengthscale to use for this problem is the radial footprint of the bump, a. Let

$$r' = \frac{r}{a}$$

$$t' = \frac{K}{a^2} t$$

From this rescaling, it follows:

$$V_0' = \frac{a}{K} V_0$$

$$a' = \frac{a}{a} = 1$$

$$a_0' = \frac{a_0}{a}$$

$$x_v' = \frac{x_v}{a}$$

$$y_v' = \frac{y_v}{a}$$

$$\psi' = \frac{\psi}{K}$$

We can use our scaled variables to re-express the energy equation

$$\mathrm{KE} = \frac{1}{2}\, \mathrm{h}\rho \int \psi\left(\vec{\nabla}\psi \cdot n\right) \mathrm{dS}$$

$$\mathrm{KE} = \frac{1}{2}\mathrm{h}\rho \int \mathrm{K}\psi'\left(\frac{1}{a_0}\,\nabla'\,\mathrm{K}\psi'\cdot\hat{n}\right) a_0 \,\mathrm{dS}'$$

$$\mathrm{KE} = \frac{1}{2}\mathrm{h}\rho\mathrm{K}^2 \int \psi'\left(\vec{\nabla}'\,\psi'\cdot\hat{n}\right) \mathrm{dS}'$$

And divide by Boltzmann's constant to scale our energy in units of Kelvins

$$\frac{\mathrm{KE}}{K_B} = \frac{1}{2}\,\frac{\mathrm{h}\rho\mathrm{K}^2}{K_B} \int \psi'\left(\vec{\nabla}'\,\psi'\cdot n\right) \mathrm{dS}' = \frac{1}{2}\,T_0 \int \psi'\left(\vec{\nabla}'\,\psi'\cdot n\right) \mathrm{dS}' \qquad (31)$$

$$T_0 = \frac{\mathrm{h}\rho\mathrm{K}^2}{K_B} \simeq 313\mathrm{K}$$

Energy Landscapes

Using equation (30) scaled in the form of (31), we can calculate the energy difference produced by a vortex pair moving along the bump and into the flat. Figure 3.10 shows many such paths for $a = 100$nm with different values of V_0, θ_b, and ϕ_v. The independent variable, r_v, refers to the radial distance from the center axis of bump, scaled to the bump footprint radius.

$$V_0 = .1 \frac{m}{s}, \theta_b = \frac{\pi}{6}$$

$$V_0 = .032 \frac{m}{s}, \theta_b = \frac{\pi}{6}$$

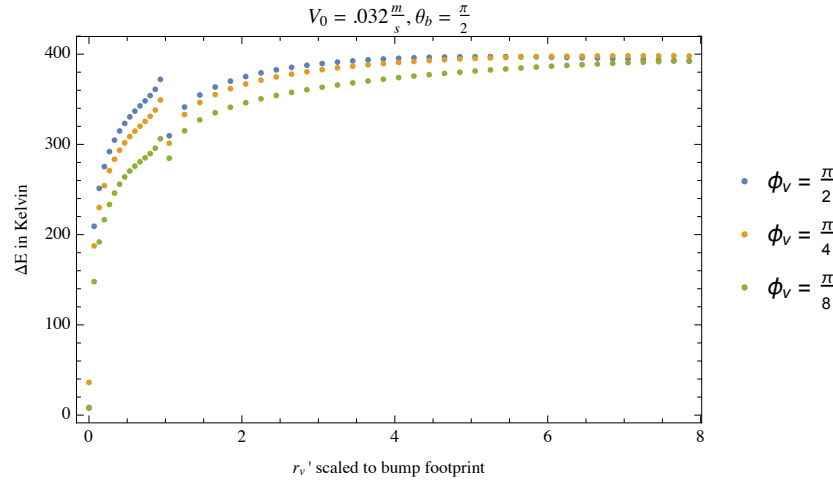$$V_0 = .1 \frac{m}{s}, \theta_b = \frac{\pi}{2}$$
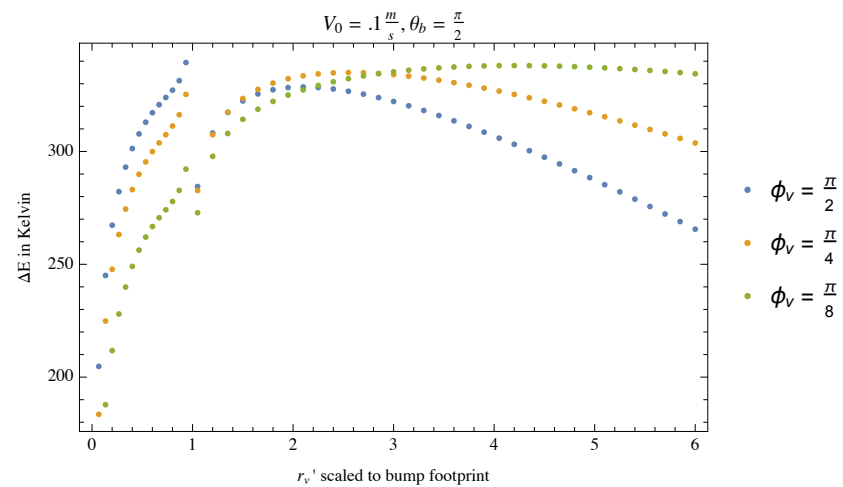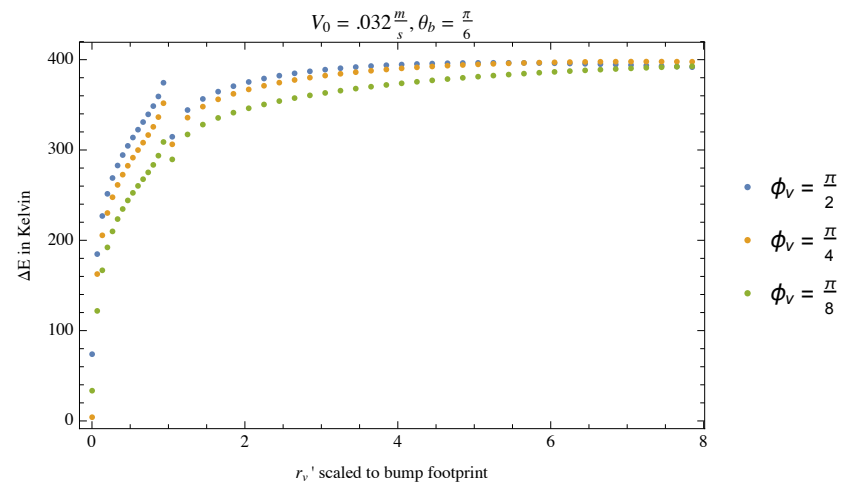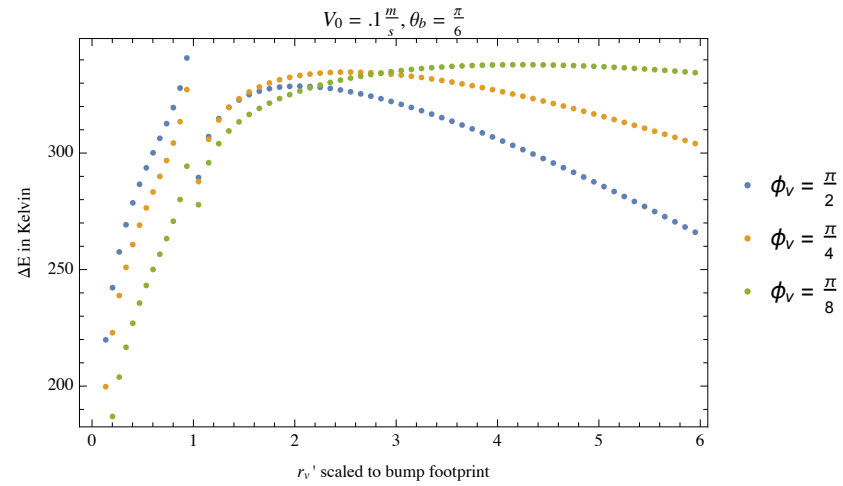
Figure 3.10: Values of kinetic energy difference created by a vortex pair plotted against radial distance from the central axis of the bump (in units of bump radial footprints) for various values of V_0 and θ_b (displayed in the plot titles) and ϕ_v (displayed in the plot legends).

The plots in Figure 3.10 invite a few notable observations. There is a substantial gap in energy difference at the boundary of the bump, which might be able to weakly pin vortices (at least in the radial direction). Furthermore, an energy barrier seems to be present in the flat, like there was for the case of the obstruction. It looks like this barrier will be closest and weakest at $\phi_v = \frac{\pi}{2}$, which was also observed with the obstruction. However, it looks like the bump energy path will be greatest at $\phi_v = \frac{\pi}{2}$. θ_b does not seem to strongly affect the energy difference once the vortex pair moves into the flat. We can further investigate this energy landscape by plotting energy contours in the flat for different values of V_0 for $\theta_b = \frac{\pi}{6}$, $a = 100$nm. These contour plots are shown in Figure 3.11. Because of symmetry, the second quadrant of the energy landscapes will look the same as the first quadrant
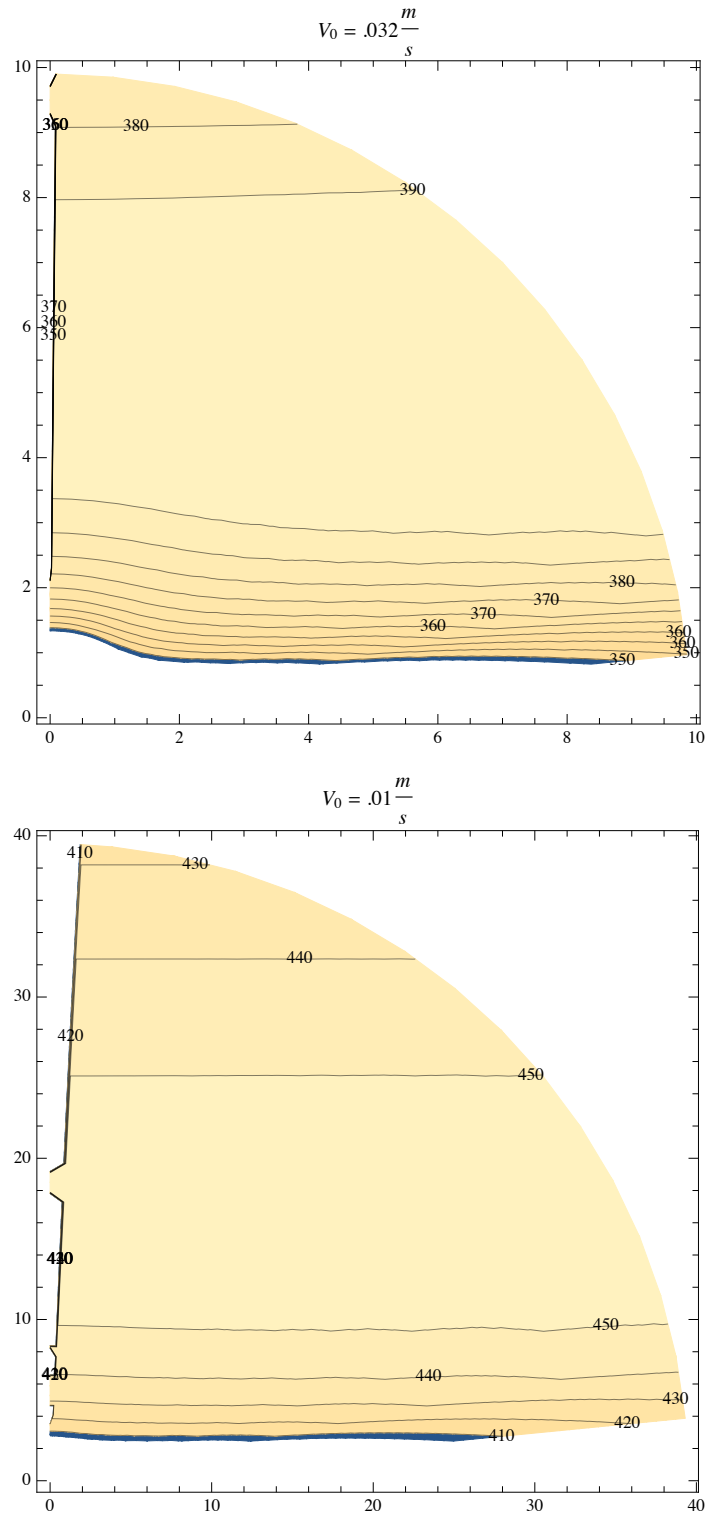
mirrored about the y-axis.

$$V_0 = .32 \frac{m}{s}$$

$$V_0 = .1 \frac{m}{s}$$
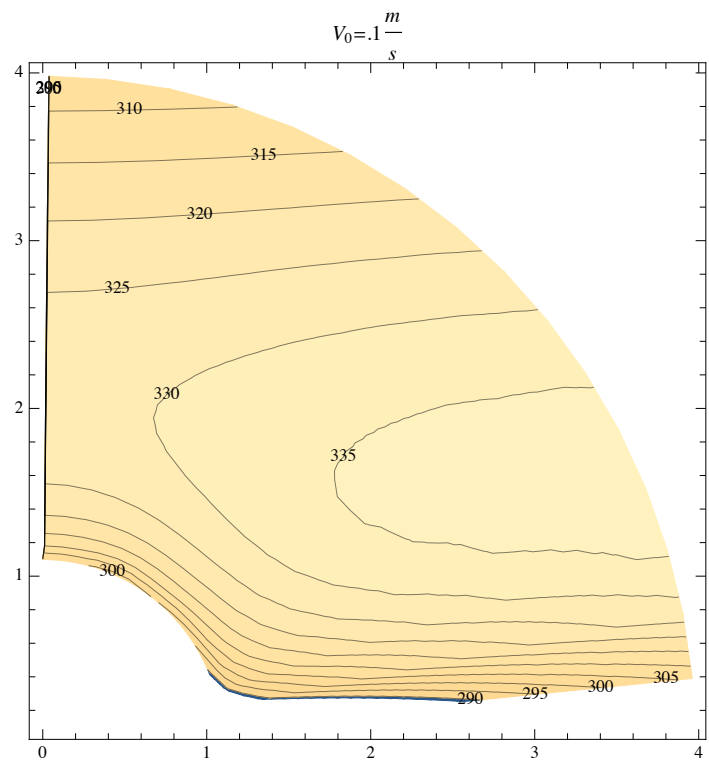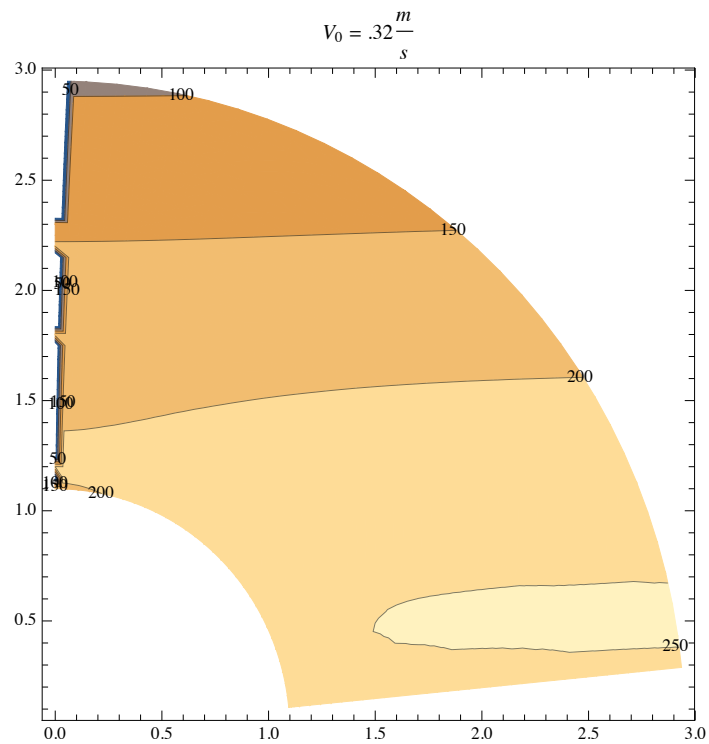
Figure 3.11: Contour plots of energy difference from a vortex pair with the
negative vortex at (x_v, y_v), the positive vortex at $(x_v, -y_v)$. The x- and y-

axes represent x_v and y_v, in units of the bump footprint. The energy differ-

ence, labeled by the contours, is in units of Kelvin.

Far from the bump, these energy difference values are similar to those

obtained from the obstruction case (as one can see by comparing Figures

3.11 and 2.5). These plots clearly show that the lowest energy escape route

for the vortices will be along the y-axis, i.e. where $\phi_v = \frac{\pi}{2}$. Furthermore, it

appears that a larger velocity will create a smaller, closer energy barrier, as

it did for the obstruction case.

Energy Barrier Analysis

We can analyze the behavior of the energy barrier for the bump in the same

way that we did for the case of the obstruction, by plotting its contours in

the space of varying background flow and bump size. In order to compare

this analysis the obstruction results from Figures 2.6 and 2.7, we can scale

this problem into the following time and length scales that were used for

the obstruction:

$$r' = \frac{r}{a_0}$$

$$t' = \frac{K}{a_0{}^2} t$$

$$V_0' = \frac{a_0}{K} V_0$$

$$a' \; = \; \frac{a}{a_0}$$

Using this scaling, we can contour plot the height of the energy barrier as a function of scaled background flow speed and scaled bump footprint size, as shown in Figure 3.12 for the case $\theta_b = \frac{\pi}{6}$, which should be a realistic bump shape.
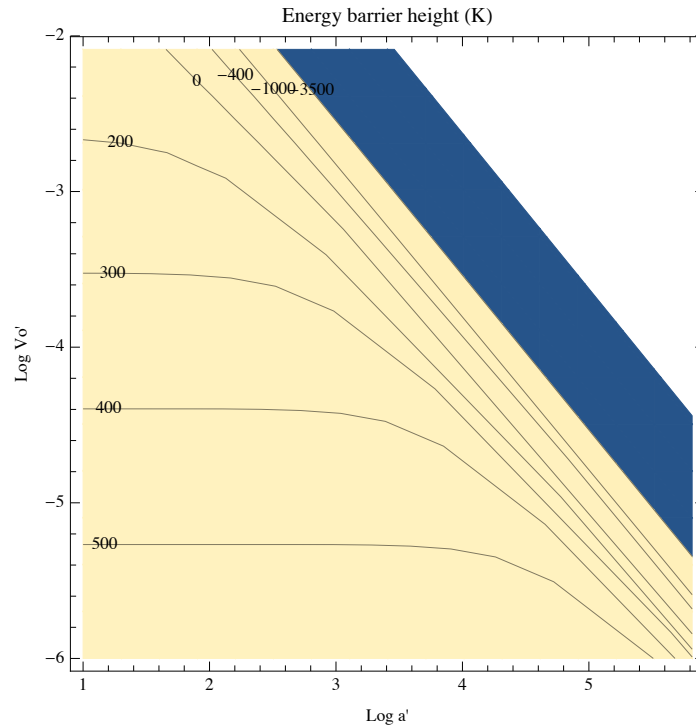

Figure 3.12: Contour plot of the height of the energy barrier for a bump of $\theta_b = \frac{\pi}{6}$. V_0' is the background flow scaled to the speed of sound in the fluid and a' is the radial footprint of the bump scaled to core sizes.

Comparing Figure 3.12 to 2.7, it appears that the energy barriers for the bump and obstruction follow a very similar pattern in this parameter space, but the energy barriers for the bump appear to be slightly higher in the low

bump size, low velocity region and slightly lower in the large bump size, higher velocity region. We can explicitly calculate the difference in energy barrier between the two configurations, as plotted in Figure 3.11. This figure shows that the bump has a higher energy barrier for lower background flow velocities and defect sizes, but the obstruction has a higher energy barrier in the limit of high velocity and large defect size. There is a small class of configurations, indicated by the "0" contour in Figure 3.13, for which the barriers will have equal height. This class of solutions can be expressed by equation (32).

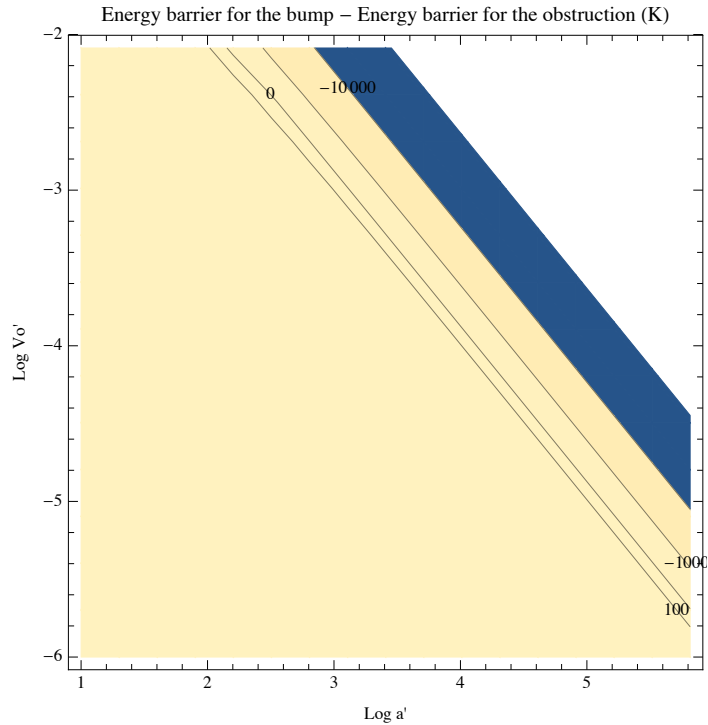$$V_0' = -1.25 * 10^{-8} * a' + 0.0041 \qquad (32)$$

Figure 3.13: Contour plot of the difference in heights of the energy barriers for a bump of $\theta_b = \frac{\pi}{6}$ and the case of the complete obstruction.

We can also look at the position of the energy barrier for the case of the bump. The log of the energy barrier position is plotted in 3.14 for the same parameter space.
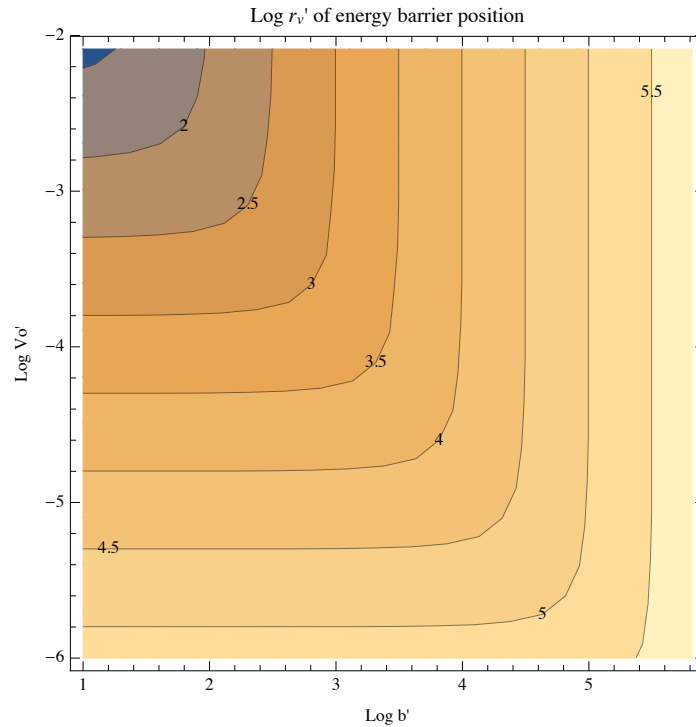

Figure 3.14: Contour plot of the log of the radial position of the energy barrier. V_0' is the background flow scaled to the speed of sound in the fluid and a' is the radial footprint of the bump scaled to core sizes.

Comparing to Figure 2.6, the energy barrier position for the bump appears to follow a similar pattern as the energy barrier position for the obstruction. We can explicitly subtract the log of the positions of the energy barriers for the bump and obstruction case, and this is shown in Figure 3.15. It appears that the obstruction always has an energy barrier that is further away than the energy barrier for the bump. This is probably due to the fact that for the

obstruction case, each individual vortex has to move away from the dipole binding potential due to its oppositely quantized image vortex inside the obstruction; whereas for the bump case, the images on the flat have 0 net circulation, and will therefore not attract the real vortex with a Magnus force.
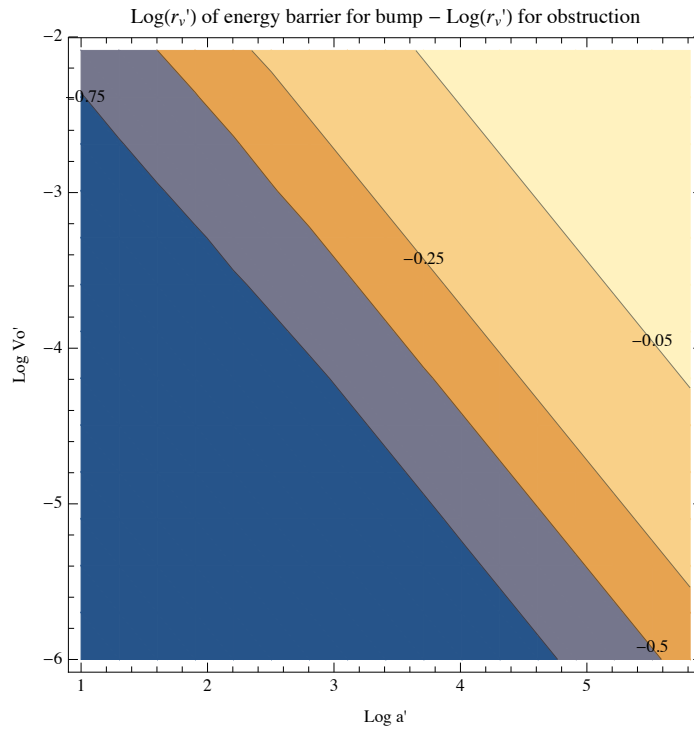

Figure 3.15: Contour plot of the difference of the log of the radial positions of the energy barrier. V_0' is the background flow scaled to the speed of sound in the fluid and a' is the radial footprint of the bump scaled to core sizes.

Chapter 4: Conclusion

With this project, we have solved Laplace's equation for both a background and vortex flow over a spherical bump around a flat plane with an approxi-

mately 2D superfluid ^{4}He film through a combination of numerical and analytical methods. We have numerically found an exact result for image solutions to Laplace's equation for a vortex on or near a bump that suggests an analytic solution is possible. We have calculated energy landscapes and identified energy barriers to vortex pair nucleation along a line perpendicular to the background flow around a bump and obstruction to flow. We have found that energy barriers decrease with larger background flow velocities and larger defect sizes, and that energy barrier positions move closer for larger velocities, and further away for larger defect sizes. We have identified a linear relationship between background flow and defect size where the obstruction and bump share the same energy barrier. For higher flows and larger sizes than this, the obstruction will have a larger energy barrier, whereas the bump will have a larger barrier for lower flows and sizes. Furthermore, the bump will always have a closer energy barrier than the obstruction, probably due to the fact that for a single real vortex, the image vortices on the flat underneath the bump do not have a net circulation, unlike the case of the obstruction, which matches each real vortex with an oppositely quantized image vortex that will exert an attractive Magnus force on the real vortex. We have also found that vortices may be weakly pinned to the boundary of the bump.

Using this framework, as well as previous work done by the Quantum Fluids Group, it should be possible to determine whether or not observed dissipation in the Stimulated Condensation Resonator and cavity resonator could have been caused by quantum turbulence around surface defects.

Previous work by Wilson and Ellis demonstrated different peak background flow velocities needed decelerate drift flow at different temperatures. [G.] If the resonator chamber were scanned microscopically, we could determine the precise size and structure of defects; along with our model, this could allow us to confirm whether or not the dissipation is caused by thermally excited vortex nucleation. With this microscopic scanning, we could also check if dissipation could be caused by vortices nucleated by quantum tunneling, as suggested by Pramudya. [H.]

Our model shows what level of energetic excitation is needed to nucleate vortex pairs for any appropriate defect size and background flow speed. With further investigation, this model may be able to quantitatively explain dissipation in 2D film flows of superfluid ^{4}He.

References

A. L.D. Landau, J. Phys. USSR, Vol.5 (1941) p.71.

B. Anand Swaminathan. Vortex Dissipation in Superfluid Third Sound Flows. Undergraduate Honors Thesis, Wesleyan University, Middletown, CT, 2009.

C. Nick Jackson. Dynamic Vortex Drag. Undergraduate Honors Thesis, Wesleyan University, Middletown, CT, 2009.

D. Sergei Dukarov, Aleksandr Kryshtal and Vladimir Sukhov (2015). Surface Energy and Wetting in Island Films, Wetting and Wettability,

Dr. Mahmood Aliofkhazraei (Ed.), InTech, DOI: 10.5772/60900. Available from: https://www.intechopen.com/books/wetting-and-wettability/surface-energy-and-wetting-in-island-films

E. S.S. Daryadel, et al., Dynamic response of glass under low-velocity impact and high strain-rate SHPB, J. Non-Cryst. Solids (2015), http://dx.doi.org/10.1016/j.jnoncrysol.2015.10.043 Academic paper (PDF): Dynamic response of glass under low-velocity impact and high strain-rate SHPB compression loading. Available from: https://www.researchgate.net/publication/283788988_Dynamic_response_of_glass_under_low-velocity_impact_and_high_strain-rate_SHPB_-compression_loading [accessed Apr 12, 2017].

F. Llewellyn Smith, Stefan G. (2002). Scattering of acoustic waves by a superfluid vortex. Journal of Physics A: Mathematical and General, 35, 3597. doi: 10.1088/0305-4470/35/16/302. UC San Diego: Retrieved from: http://escholarship.org/uc/item/8c43f1n3

G. "Excitation and Relaxation of Film Flow Induced by Third Sound"
F. M. Ellis and C. Wilson, J. Low Temp. Phys., 113, 411 (1998)

H. "Improvements in the Construction and Detection Electronics of a Third Sound Resonator Used for the Observation of Stimulated Condensation in Superfluid 4He" Yudhiakto Pramudya, Ph.D. thesis, Wesleyan University, Middletown, CT, 2013